1 **Title Page**

2 **An atypical F-actin capping protein modulates cytoskeleton behaviors crucial to colonization of**

3 ***Trichomonas vaginalis***

4 Kai-Hsuan Wang[1, #], Jing-Yang Chang[1, #], Fu-An Li[2], Yen-Ju Chen[1], Kuan-Yi Wu[1], Tse-Ling Chu[3],

5 Jessica Lin[3], and Hong-Ming Hsu[1, *]

6 [1]Department of Tropical Medicine and Parasitology, College of Medicine, National Taiwan University,

7 Taipei, Taiwan 100233.

8 [2]The Proteomic Core, Institute of Biomedical Sciences, Academia Sinica, Taipei, Taiwan 11529.

9 [3]Taipei First Girls High School, Taipei, Taiwan 100006.

10 [#]These authors contributed equally to this work.

11 *Address correspondence to:

12 Hong-Ming Hsu, Department of Tropical Medicine and Parasitology, College of Medicine, National

13 Taiwan University, Taipei, Taiwan 100. Tel: 886-2-23123456 ext. 88260; Fax: 886-2-23915294; E-

14 Mail: hsuhm@ntu.edu.tw

15

16 **Running title:** CP regulates *T. vaginalis* colonization

17

Abstract

Cytoadherence and consequential migration are crucial for pathogens to establish colonization in the host. In contrast to the nonadherent isolate of *Trichomonas vaginalis*, the adherent one expresses more actin-related machinery proteins with more active flagellate-amoeboid morphogenesis, amoeba migration, and cytoadherence, activities that were abrogated by an actin assembly blocker. By immunoprecipation coupled with label-free quantitative proteomics, an F-actin capping protein (*Tv*FACPα) was identified from the actin-centric interactome, with an atypically greater binding preference to G-actin than F-actin. *Tv*FACPα partially colocalized with F-actin at the parasite pseudopodia protrusion and formed the protein complexes with α-actin through its c-terminal domain. Meanwhile, *Tv*FACPα overexpression suppresses F-actin polymerization, amoeboid morphogenesis, and cytoadherence in this parasite. Ser^2 phosphorylation of *Tv*FACPα enriched in the amoeboid stage of adhered trophozoites was reduced by a CKII inhibitor. The site-directed mutagenesis and CKII inhibitor treatment revealed that Ser^2 phosphorylation acts as a switching signal to alter *Tv*FACPα actin-binding activity and consequent actin cytoskeleton behaviors. Through CKII signaling, *Tv*FACPα also controls the conversion of adherent trophozoite from amoeboid migration to flagellate form with axonemal motility. Together, CKII-dependent Ser^2 phosphorylation regulates *Tv*FACPα binding actin to fine-tune cytoskeleton dynamics and drive crucial behaviors underlying host colonization of *T. vaginalis*.

Keywords: Actin capping protein/ Actin Cytoskeleton/ Cytoadherence/ Colonization/ *Trichomonas vaginalis*

Introduction

Trichomonas vaginalis is a pathogenic protist causing trichomoniasis which is one of the most prevalent non-viral sexually transmitted diseases, with approximately 180 million new infections worldwide annually (1).

A successful pathogenic infection includes cytoadherence to establish colonization, followed by migration for population spread. Numerous studies on *Trichomonas vaginalis* have focused on the cytoadherence mechanism in adhesion molecules, like cadherin (2), rhomboid protease (3), legumain protease (4), BAP proteins (5), *Tv*AD1 protein (6), and surface-expressed hydrogenosomal proteins (7, 8, 9, 10). However, the effects of these reputed adhesins in cytoadherence are limited when analyzed by the gain- or loss-of-function assays (2-10). Thus, we postulated that the cytoadherence of *T. vaginalis* might be regulated by pathways other than adhesion molecules. In mammalian adhesion cells, transmembrane integrins link peripheral focal protein complexes underneath the cell membrane for focal adhesion, which is the site that connects the extracellular matrix to transmit traction forces required for cell migration and activates downstream signaling followed by local cytoskeleton reorganization (11, 12, 13). A few studies have used ligand competition or antibody neutralization to demonstrate the involvement of integrin-like molecules in the cytoadherence of *T. vaginalis* (14, 15, 16). Recently, the adherence of clinical *T. vaginalis* isolates to the plastic surface or host cells was

shown to be influenced by an actin polymerization blocker (17), implying that the actin cytoskeleton might coordinate cytoadherence in *T. vaginalis*, but the regulatory mechanism was unknown.

Furthermore, flagellate-amoeboid transition immediately after contact with a solid surface or human vagina epithelium cells (*h*VECs), is another striking feature in adherent isolates of *T. vaginalis* (18). Upon morphological transformation, the free-swimming flagellar trophozoite converts to an adherent trophozoite that crawls over a solid surface by pseudopodia-like protrusions referred to as amoeboid migration. A similar flagellate-amoeboid transition was observed in the pathogenic amoeba, *Naegleria fowleri.* This free-living trophozoite builds lamellipodia-like protrusions for phagocytosis and migration driven by actin cytoskeleton machines (19), in which actin expression correlates with its virulence (20).

The actin cytoskeleton is a complex network of actin filaments and actin-associated proteins that shape cell morphology, drive cellular locomotion, and confer cell adhesion (21, 22, 23). The globular actin monomer (G-actin) polymerizes into filamentous actin polymers (F-actin), which are further organized into bundles or branched into three-dimensional networks for complicated cytoskeleton activities. In the polarized F-actin filament, growth initiates from the assembly of the Arp2/3 nucleation complex (24), then G-actin is continuously added at the fast-growing barbed end or dissociated from the pointed end (25). The cellular actin cytoskeleton dynamics are tightly modulated by a variety of accessory effectors for actin polymerization, depolymerization, branching, and reorganization (26). In high eukaryotes, F-actin capping protein (CP) is heterodimerized from α (CPα) and β (CPβ) subunits to form a mushroom-shaped structure capping the fast-growing barbed end of F-actin to block off G-actin access and subsequent polymerization. The C-terminal regions of CPα and CPβ form as two tentacles to bind actin (27, 28, 29). A set of regulatory proteins binds to the barbed end of F-actin to prevent the binding of CP, or several proteins directly bind CP to spatially guide subcellular localization or allosterically alter actin capping activity for instant regulation of cytoskeleton remodeling (30, 31).

Post-translational modifications like phosphorylation and acetylation on the interacting interface within the c-terminal tentacle of CPβ alter the actin-binding dynamics (32). Human CPα forms a protein complex with Casein kinase II-interacting protein (CKIP-1) and Casein kinase II (CKII). CKII phosphorylates the Ser^9 of CPα coordinating CKIP-1 to inhibit capping activity, but this inhibitory effect seems to be independent of Ser^9 phosphorylation (33, 34). The capacity of CP binding actin filaments is tightly regulated in a spatial or allosteric manner to fine-tune the actin assembly dynamics in cells.

The mechanisms of actin cytoskeleton regulation in *T. vaginalis* have not been fully elucidated. *Tv*Fimbrin1 protein (*Tv*Fim1) has been identified *in vitro* to accelerate actin assembly and *in vivo* to co-localize with F-actin at the cell membrane periphery in the pseudopod-like structures of *T. vaginalis* upon phagocytosis or migration (35). In this study, a putative F-actin capping protein subunit α (*Tv*FACPα) was identified and characterized from the α-associated protein complexes in *T. vaginalis*.

Results

Differential morphogenesis, cytoadherence, and motility of *T. vaginalis*

The differential host-parasite interaction between nonadherent T1 and adherent TH17 isolates was evaluated by the cytoadherence, morphogenesis, and motility. CFSE-labeled trophozoites were co-cultured with the *h*VECs monolayer at MOI of 2:1. Post 60-min infection, ~80% of TH17 but little T1 trophozoites bound to the *h*VECs monolayer (Figure 1A). Most T1 trophozoites maintained an oval-shaped flagellate form, but ~60% of TH17 trophozoites transformed into a flat disk or irregular ameboid form and tightly adhered to the slide surface (Figure 1B). To further observe the dynamics of host-parasite interaction, the trophozoites co-cultured with *h*VECs were monitored by time-lapse imaging (Figure 1C and Videos 1 and 2), showing that nonadherent T1 trophozoites maintained a flagellate form and swam by flagellar locomotion only randomly coming into contact with the *h*VECs. By contrast, adherent TH17 trophozoites rapidly transformed into an amoeboid form within 10 min of contact with the glass slide and crawled toward *h*VECs via pseudopod-like protrusions, referred to as amoeboid migration. In contrast to *T. vaginalis* nonadherent isolate, the adherent isolate displayed more active cytoadherence and amoeboid morphogenesis and migration.

Fig.1

4
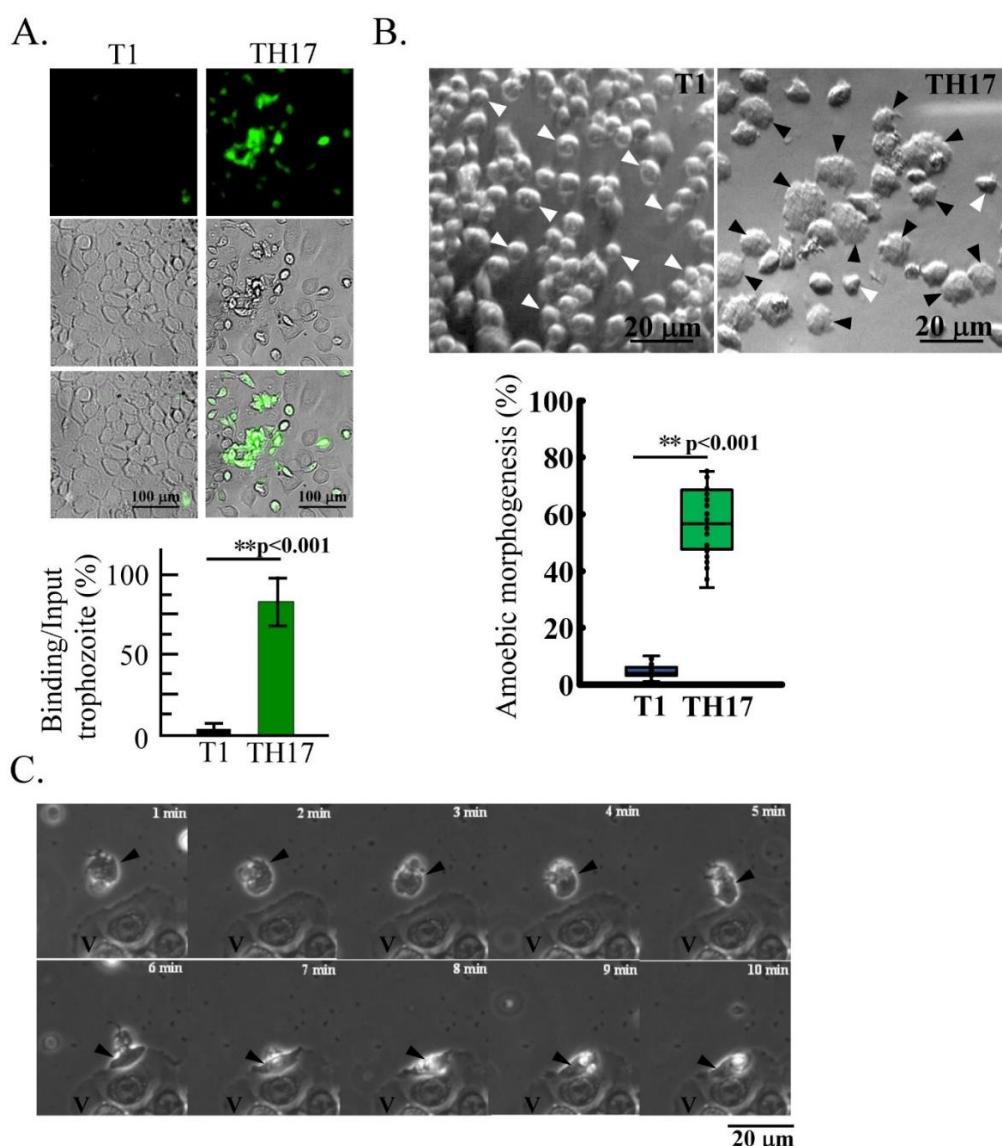
111 **Figure 1. Differential cytoadherence, morphogenesis, migration mode of *T. vaginalis.*** A
112 variety of behaviors were observed in the nonadherent (T1) and adherent (TH17) isolates. (A.)
113 The CFSE-preloaded trophozoites were cultured with *h*VECs, then fixed 1 hr post-infection.
114 The cytoadherence capacity was evaluated by the ratio of binding versus input trophozoites
115 as shown in the histogram. Scale bar: 100 μm. (B.) The ratio of T1 or TH17 trophozoites at
116 the amoeboid form was measured in ~600 trophozoites from 12 random microscopic fields
117 as shown in the box and whisker plot. The black and white arrowheads respectively indicate
118 the representative amoeboid and flagellate trophozoites. Scale bar: 20 μm. (C.) TH17
119 trophozoite (black arrowhead) was co-cultured with *h*VECs (V). The dynamics of ameboid
120 migration and morphogenesis were recorded by time-lapse imaging at one frame per 15 sec
121 over 10 min. Scale bar: 20 μm. All experiments were repeated three times. Data in histogram
122 are presented as mean ± SEM. Statistical significance with p-value for each group of data
123 was analyzed by Student's t-test as indicated (n=3, $P < 0.01$**, $P < 0.05$*, and ns, no
124 significance).

125

126 **(Please see the attached Video 1)**
127 **Video1 Dynamics of amoeboid morphogenesis and migration in the adherent isolate of *T.***
128 ***vaginalis.*** The trophozoites from TH17 adherent isolate were co-cultured with *h*VECs. The dynamics
129 of trophozoite activities were recorded by time-lapse imaging at the capturing rate of one frame per 30
130 sec over time as defined.

131

132 **(Please see the attached Video 2)**
133 **Video2 Dynamics of migration in the nonadherent isolate of *T. vaginalis*.** The trophozoites from
134 nonadherent T1 isolate were co-cultured with *h*VECs. The dynamics of trophozoite activities were
135 recorded by time-lapse imaging at the capturing rate of one frame per 30 sec over time as defined.

136

137

138 **Differential expression of actin-related proteins in *T. vaginalis***
139 Cytoadherence and migration in *T. vaginalis* correlate with actin cytoskeleton (17, 35), therefore,
140 the expression of α-actin and α-actinin, the respective major component and actin bundle linker protein
141 in the cytoskeleton were investigated. The expression of α-actin and α-actinin varied between isolates
142 and was higher in adherent TH17 and T016 isolates compared to nonadherent T1, special in a fresh
143 adherent isolate from a clinical vaginitis patient (Figure 2A). The overexpression of HA-*Tv*actin in a
144 nonadherent isolate did not induce amoeboid morphogenesis or cytoadherence (Figure 2-Figure
145 Supplement 1), suggesting that α-actin might be determinant but insufficient to confer cytoadherence
146 in a nonadherent isolate. Additionally, no detectable α-actin on the adherent parasite surface indicates
147 that α-actin is unlikely to act as an adhesion molecule (Figure 2-Figure Supplement 2).
148 The immunostaining of α-actin was more intense in TH17 than T1 trophozoites and detected in
149 tiny punctate or short bundles in the cytoplasm of the free-swimming flagellate TH17 but in dense fine

150   networks in the cytoplasm with sporadic clumps underneath the plasma membrane of the amoeboid-
151   adhered TH17. However, the expression of α-actin and α-actinin was similar between the two forms of
152   TH17 trophozoites according to western blotting (Figure 2C). The validated phalloidin binding sites
153   are conserved in α-actin of *T. vaginalis* (Figure 2-Figure Supplement 3) (36). F-actin was double-
154   stained by TRITC-conjugated phalloidin and anti-α-actin antibody (Figure 2D), showing prominent F-
155   actin and α-actin signals concentrated in the juxtanuclear region, referred to as perinuclear actin cap
156   (39), with intense staining underneath the cell membrane of the leading edge in protrusive pseudopods,
157   and less intense staining in the cytoplasm. The signal colocalization of α-actin and phalloidin had a
158   Pearson's correlation coefficient value of 0.95 (Figure 2D, bottom panel). To evaluate F-actin assembly
159   in cells, G-actin, F-actin, and co-sediments were fractionated, and western blotting analysis revealed
160   an F-actin ratio of ~70% in the adherent isolate and ~30% in the nonadherent one (Figure 2E), similar
161   to α-actinin. It is speculated that F-actin polymerization is more active in the adherent than the
162   nonadherent isolate, and that the actin assembly pattern is also distinct.

Fig. 2
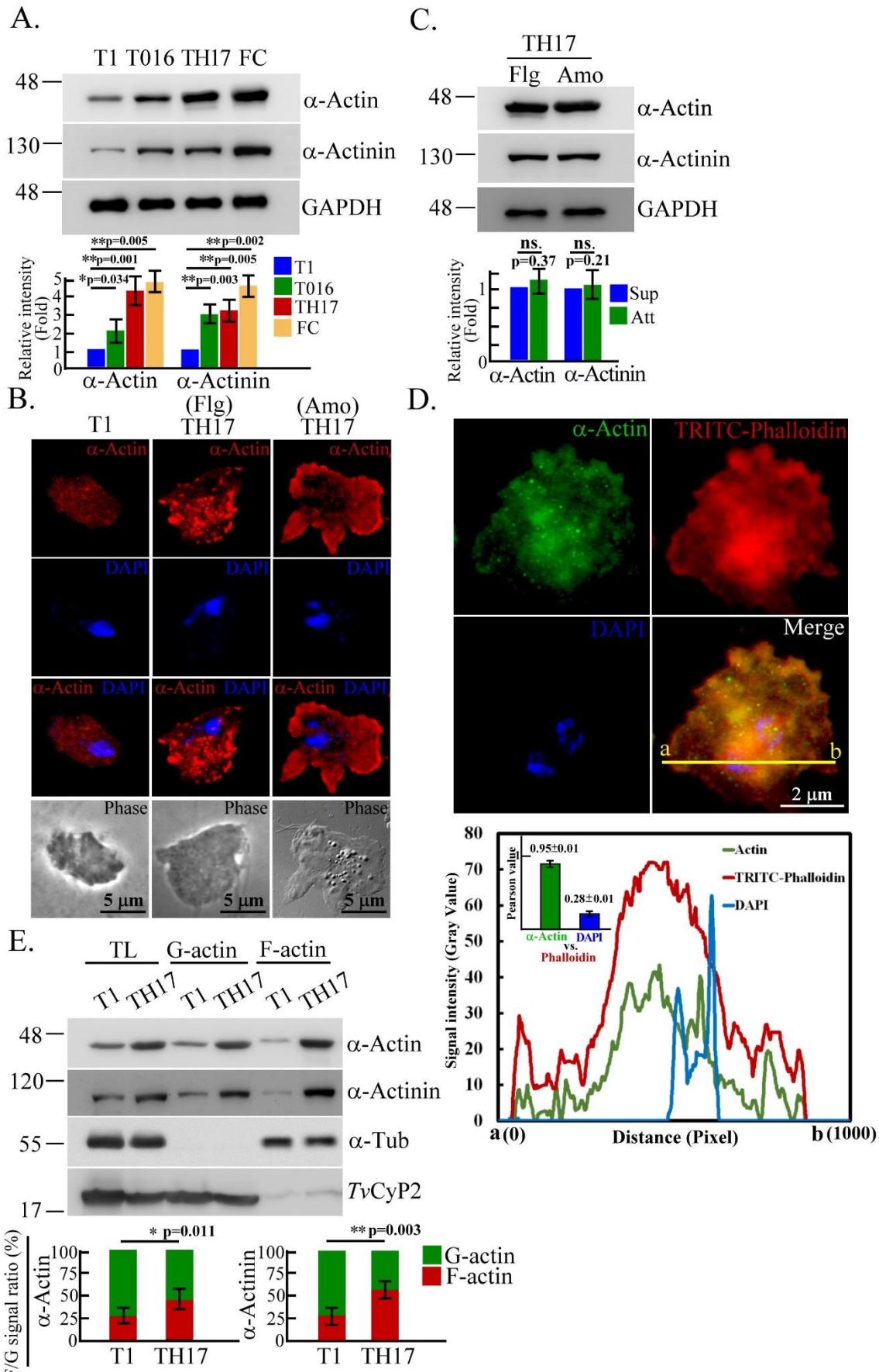
Figure 2. Differential expression of actin-based machinery proteins in *T. vaginalis*. (A.) The total lysates from T1, T016, TH17, and a fresh clinical isolate (FC) were subjected to western blotting. (B., C.) TH17 flagellates (Flg) trophozoites suspended in the medium or amoeboid (Amo) trophozoites adhered to the glass surface were sampled for IFA as shown in (B.) or western blotting as shown in (C.). Scale bar in (B.), 5 μm. (D.) TH17 cultured on a glass slide and fixed for IFA double-staining with anti-α-actin antibody and TRITC-conjugated phalloidin. Signal colocalization was evaluated by a plot profile analysis to show the signal intensity distribution on the yellow line between a and b sites as shown in the diagram. The colocalization of phalloidin with α-actin or DAPI was evaluated by Pearson's correlation coefficient as shown in the inset histogram. Data are presented as mean ± SEM. Scale bar: 2 μm. (E.) The protein lysates of actin fractionation from T1 and TH17 trophozoites were examined by western blotting. The ratio of indicated protein signal in F-actin and G-actin fractions was analyzed as shown in the histogram. All experiments were repeated three times. Data in histogram are presented as mean ± SEM. Statistical significance with p-value for each group of data was measured by Student's t-test as indicated (n=3, $P< 0.01$**, $P< 0.05$ **, and ns, no significance).

Actin-based morphogenesis, migration, and cytoadherence in *T. vaginalis*.

Latrunculin B (LatB) binding sites are conserved in α-actin of *T. vaginalis* (Figure 2-Figure Supplement 3), therefore adherent TH17 trophozoites were treated with LatB to study the role of F-actin in cytoskeleton behavior and cytoadherence. LatB treatment reduced the ratio of F-actin assembly (Figure 3A) and morphogenesis (Figure 3B) in the parasite compared to the DMSO control, as well as decreasing the wound closure rate (Figure 3C) and cytoadherence 60-min post-infection (Figure 3D), showing that F-actin disorder retarded morphogenesis, amoeboid migration, and cytoadherence of this parasite. To rule out the effects from the reputed adhesion molecules (2, 7, 10), the expression of AP65 and PFO (Figure 3E), and their surface distributions (Figure 3F) were analyzed, showing that there was no change in adhesion molecules in the trophozoites with or without LatB treatment. Under IFA permeation condition, hydrogenosomal colocalization of AP65 and PFO proved their surface signal specificities (7, 10). Also, the surface localization of HA-tagged Cadherin-like protein (CLP) was not affected by LatB treatment (Figure 3G). Taken together, actin polymerization is positively associated with the parasite morphological transition, amoeboid migration, and cytoadherence. Also, LatB-inhibited cytoadherence might be independent of adhesion molecules.

Fig. 3

197
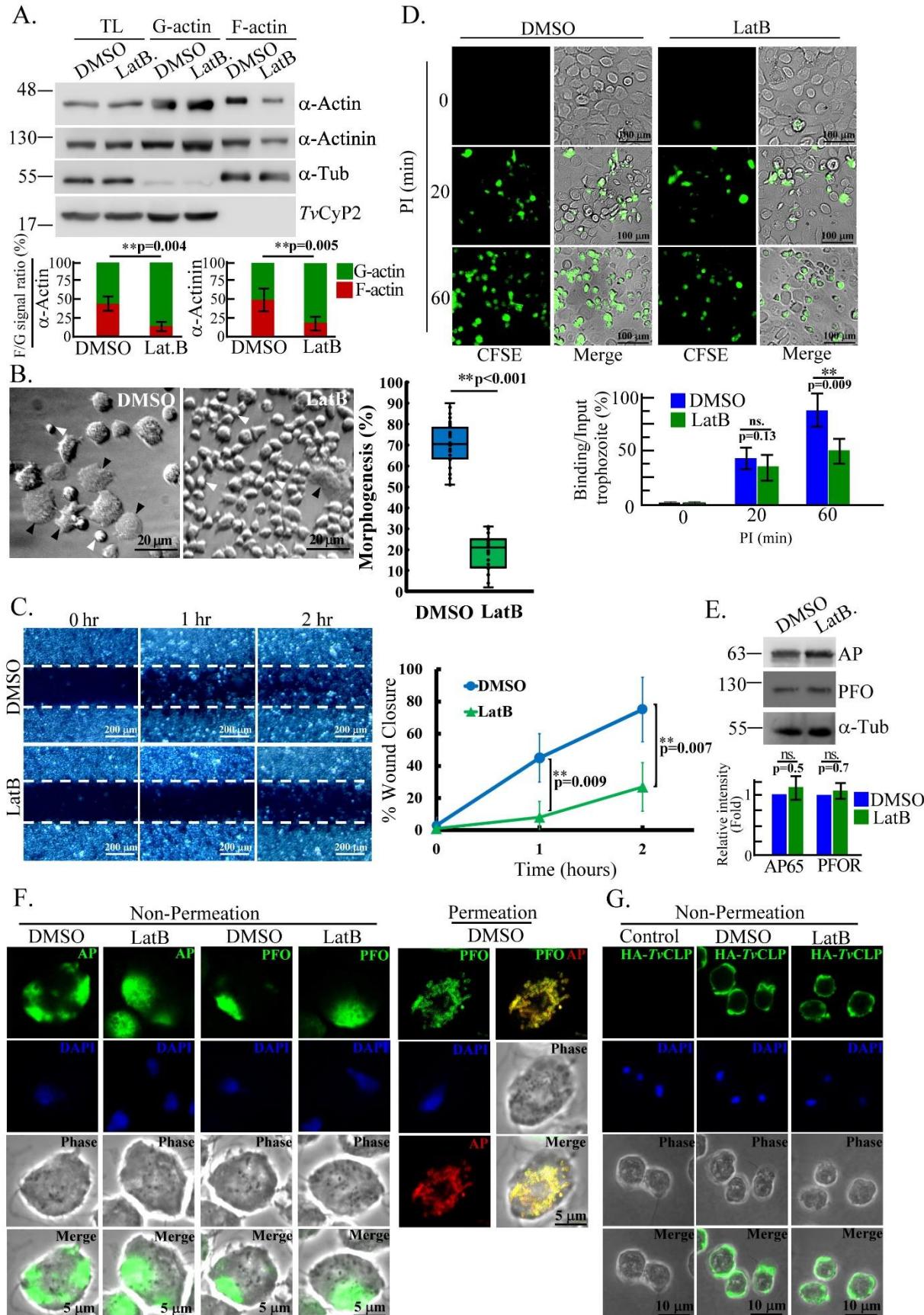
Figure 3. The dysregulation of cytoskeleton-dependent behaviors in *T. vaginalis*. TH17 adherent trophozoites pretreated with DMSO or LatB were sampled for various assays. (A.) Total lysates (TL) or protein lysates of actin fractionation were subjected to western blot. The signal ratio of F-actin versus G-actin (F/G) was measured as shown in the histogram. (B.) Trophozoite morphology was observed by phase-contrast microscopy. The proportion of trophozoites in amoeboid form was measured in 600 trophozoites from 12 random microscopic fields as shown in the box and whisker plot. The black and white arrowheads respectively indicate the representative amoeboid and flagellate forms of trophozoites. Scale bar: 20 μm. (C.) In the wound healing assay, the representative images were captured at 0, 1, and 2 hr. The wound closure rate was measured as the percentage of wound recovery area at indicated time points. The white dashed lines depict the initial wound edge. (D.) In the binding assay, the conditional trophozoites were co-cultured with *h*VECs for the time as indicated. The ratio of trophozoites binding versus input was calculated as shown in the histogram. Scale bar: 100 μm. (E.) Total lysates from conditional trophozoites were subjected to western blotting. (F.) The fixed trophozoites with or without permeation were stained by anti-PFO and anti-AP65 antibodies for IFA. Scale bar: 5 μm. (G.) The non-transgenic control and transgenic trophozoites overexpressing HA-*Tv*CLP were stained by anti-HA antibody for IFA under non-permeation conditions. Scale bar: 10 μm. All experiments were repeated three times. Data in histogram and line chart are presented as mean ± SEM. Statistical significance with p-value for each group of data was analyzed by Student's t-test as indicated (n=3, *P*< 0.01**, *P*< 0.05 **, and ns, no significance).

_Tv_FACPα as an α-actin effectors

Since α-actin is not sufficient to promote the cytoadherence in *T. vaginalis* nonadherence isolate, we attempted to identify the regulatory proteins in the α-actin-associated complexes. HA-*Tv*actin was immunoprecipitated from transgenic TH17 trophozoites and subjected to mass spectrometry analysis (Figure 4A), identifying 41 α-actin-associated proteins with an emPAI score above 0.25 or specific in the immunoprecipitant of HA-*Tv*actin (Table 1). These proteins were classified by function into multiple cellular pathways, including cytoskeleton proteins (22%), chaperones (5%), membrane trafficking and transporter (10%), protein binding or modification (7%), DNA/RNA regulation and translation (17%), metabolism enzymes (37%), and uncharacterized proteins (2%) (Figure 4- Figure Supplement 1). The top five abundant protein identified in IP proteome were listed in Figure 4B. Bait HA-*Tv*actin was identified with an emPAI score of ~9.5, an F-actin CP subunit α homolog, referred to as *Tv*FACPα (TVAG_470230), had an emPAI score of ~9.7 (Figure 4B) and 40% identified peptide coverage (Figure 4C), supporting the possibility of a strong protein-protein interaction between *Tv*FACPα and *Tv*actin. The in-silico protein sequence analysis revealed that *Tv*FACPα encodes 267 amino acids with a molecular weight of 29.1 kDa and a PI value of 5.43 and shares 17% identity and 63% similarity with CPα from high eukaryotes (Figure 4D). *Tv*FACPα contains a highly conserved

237   actin-binding domain at C-terminus spanning amino acids from 237 to 261. By a phosphorylation site

238   prediction algorithm (NetPhos 3.1 Generic phosphorylation prediction:

239   Services.healthtech.dtu.dk/service.php?NetPhos-3.1), Ser^2, Ser^{46}, Ser^{88}, Ser^{106}, and Ser^{223} were

240   predicted as CKII phosphorylation sites. The sequence of $^2SESE^5$ fits the putative CKII

241   phosphorylation motif (pS/pTDXE) possibly recognized by a phospho-CKII substrate antibody. In the

242   TrichDB database, BLAST analysis identified two CPα homologous proteins (TVAG_470230 and

243   TVAG_212270) with 32% sequence similarity (Figure 4-Figure Supplement 2) but whether they are

244   functionally redundant in this parasite remains to be studied.

245

246   **(Please see the attached Table 1 file)**

247   **Table 1. The list of *Tv*actin-interacted proteins identified by LC-MS/MS.** The proteins identified

248   by mass spectrometry with emPAI value above 0.25 or the peptides specific in the immunoprecipitant

249   of HA-*Tv*actin were listed.

Fig. 4

B. The top 5 abundance proteins identified in IP proteome
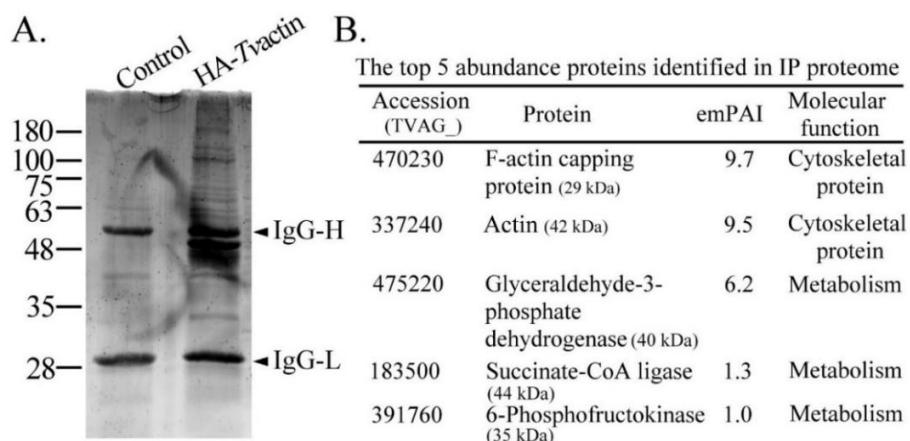
| Accession (TVAG_)	Protein	emPAI	Molecular function
470230	F-actin capping protein (29 kDa)	9.7	Cytoskeletal protein
337240	Actin (42 kDa)	9.5	Cytoskeletal protein
475220	Glyceraldehyde-3-phosphate dehydrogenase (40 kDa)	6.2	Metabolism
183500	Succinate-CoA ligase (44 kDa)	1.3	Metabolism
391760	6-Phosphofructokinase (35 kDa)	1.0	Metabolism
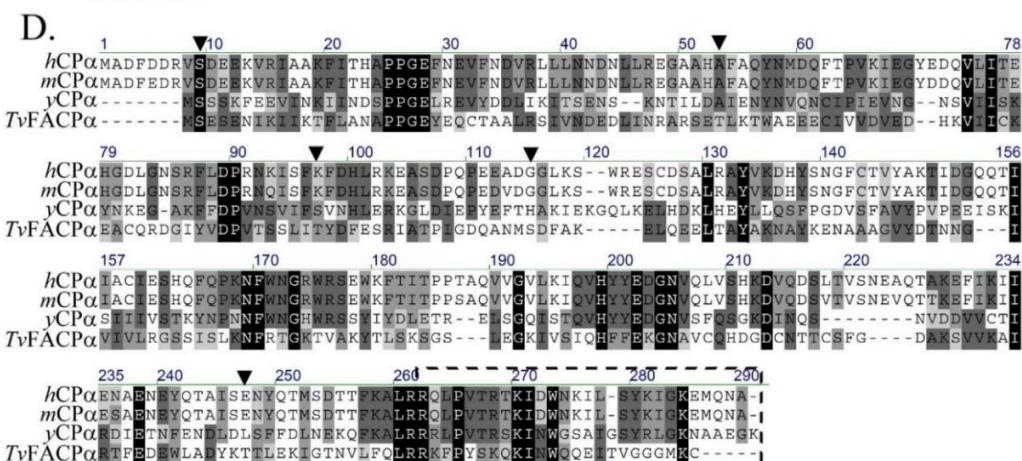
250

251 **Figure 4. Proteomic identification of actin-binding effectors.** (A.) The immunoprecipitants
252 from non-transgenic control or transgenic TH17 trophozoites overexpressing HA-*Tv*actin
253 were separated by SDS-PAGE, followed by SYPRO Ruby staining. (B.) In-gel tryptic digests
254 were processed for a label-free quantitative proteomic analysis. The top five abundant
255 proteins were listed by their emPAI in descending order. The all identified proteins were
256 summarized in Table 1. (C.) *Tv*FACPα-specific peptides identified by LC-MS/MS were
257 labeled in red to show the coverage. (D.) The full-length protein sequence of *Tv*FACPα was
258 aligned with the CPα from human (*h*CPα, P52907), mouse (*m*CPα, P47753), and yeast (*y*CPα,
259 P28495). The conserved amino acid sequences are highlighted. The predicted Casein kinase
260 II phosphorylation sites are indicated by downward arrowheads, and the actin-binding domain
261 is boxed by a black dashed line.

262
263

264 **The non-canonical interaction of *Tv*FACPα to α-actin**

265 Immunoprecipitation was performed to examine whether *Tv*FACPα forms the protein complexes
266 with α-actin in *T. vaginalis*, with two major bands at ~30 and ~32 kDa recognized by an anti-HA
267 antibody in the total lysates. A 42-kDa α-actin and a 110-kDa α-actinin band were co-
268 immunoprecipitated from the trophozoites overexpressing HA-*Tv*FACPα but not the non-transfectant
269 control (Figure 5A). To further confirm the direct interaction of *Tv*FACPα and α-actin, His-*Tv*FACPα,
270 His-△237 mutant, GST and GST-*Tv*actin were purified to homogeneity for the pull-down assay
271 (Figure 5B, left panel). When an equal amount of His-*Tv*FACPα and His-△237 were reacted with GST
272 or GST-*Tv*actin for the pull-down assay, the signal from His-*Tv*FACPα but not His-△237 was pulled
273 down with GST-*Tv*actin, showing that the c-terminal domain is vital for the direct binding of *Tv*FACPα
274 and α-actin (Figure 5B, right panel).

275 The function of *Tv*FACPα in actin assembly was analyzed by an *in vitro* polymerization assay.
276 When over ~95% G-actin polymerized into F-actin in F-buffer in the absence of His-*Tv*FACPα (Figure
277 5C left panel), F-actin polymerization ratio was only ~25% in the presence of His-*Tv*FACPα, of which
278 25% of His-*Tv*FACPα co-sedimented with F-actin. By contrast, the polymerization ratio was 75% in
279 the presence of His-△237, and less than 5% of His-△237 could be co-sedimented with F-actin (Figure
280 5C), indicating that *Tv*FACPα directly interacts with actin molecules to attenuate polymerization. Of
281 note, only 25% of *Tv*FACPα co-sedimented with F-actin but it inhibited over ~70% F-actin formation
282 in the polymerization assay, suggesting that *Tv*FACPα also binds G-actin to inhibit its polymerization.

283 To determine the kinetics of *Tv*FACPα binding G-actin and F-actin by a solid phase binding
284 immunoassay, two forms of actin were reacted with various concentrations of His-*Tv*FACPα or His-
285 △237 mutant to measure the K_d and B_{max} values (Figure 5D). The binding signal increased
286 with increasing concentration of His-*Tv*FACPα or derived mutant, and plateaued in the presence of
287 over 20 μM of His-*Tv*FACPα. The binding curves show that His-*Tv*FACPα binds F-actin with a K_d of
288 8.36 μM and B_{max} of 1.35 and G-actin with a K_d of 4.45 μM and B_{max} of 1.5. By contrast, His-△237
289 binds both F-actin and G-actin with a similar B_{max} of ~0.5, only one-third of His-*Tv*FACPα (Figure 5D

12

290   inset table). In contrast with the canonical F-actin binding preference for high eukaryotic CPα, the *in*
291   *vitro* assays demonstrated that *Tv*FACPα bound G-actin with an affinity greater than F-actin to suppress
292   actin polymerization.

Fig. 5

293
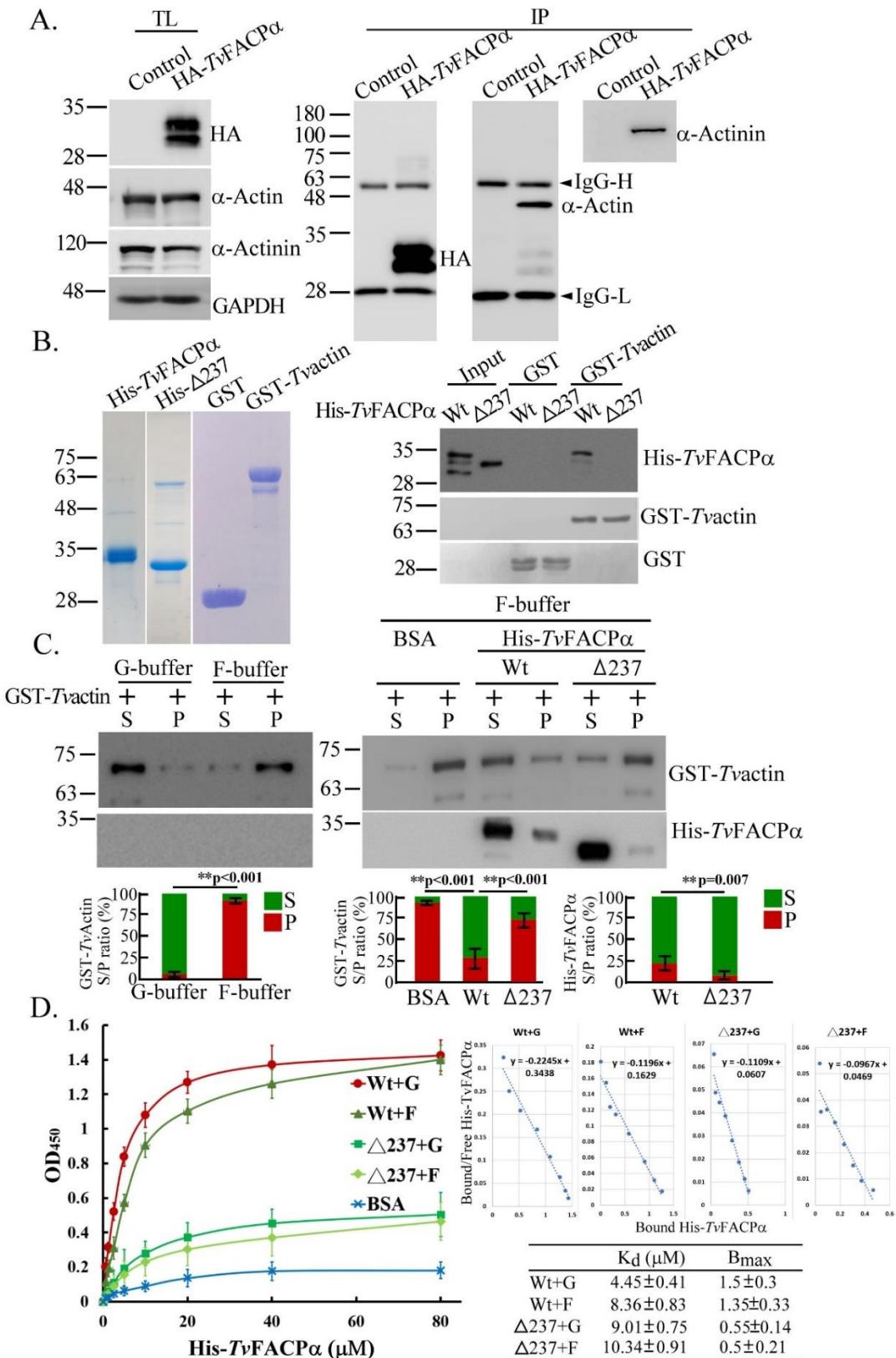
Figure 5. Direct interaction of *Tv*FACPα with G-actin and F-actin. (A.) The total lysate (TL) from non-transgenic control or transgenic TH17 trophozoites expressing HA-*Tv*FACPα was immunoprecipitated by anti-HA antibody (IP), followed by western blotting. GAPDH was detected as the loading control. (B.) The purities of recombinant His-*Tv*FACPα wild type (Wt), His-△237, GST, and GST-*Tv*actin were examined by SDS-PAGE with Coomassie blue staining (left panel). Equimolar GST or GST-*Tv*actin immobilized on glutathione beads was incubated with His-*Tv*FACPα (Wt) or His-△237 mutant for the GST pull-down assay. The pull-down samples were blotted on PVDF membrane for western blotting with anti-6×His antibody or for Ponceau S staining (right panel). 1/10 of the input protein was loaded for positive control. (C.) *In vitro* actin polymerization assay was performed to react G-actin in G- or F-buffer (left panel) or reaction in the presence of His-*Tv*FACPα, His-△237 or BSA control (right panel). After ultracentrifugation, F-actin and its associates were isolated in the pellet (P) from G-actin in the supernatant (S), then examined with western blotting by anti-α-actin or anti-6×His antibody. The signal ratio of indicated protein in the supernatant versus pellet (S/P) was quantified as shown in the histogram. (D.) The equimolar G-actin (G) and F-actin (F) coated on a 96-well microplate were incubated with various concentrations of His-*Tv*FACPα (Wt) or His-△237 (△237) mutant. The saturation binding curve is plotted by the OD_{450} absorbance against various concentrations of His-*Tv*FACPα or His-△237 mutant protein to create Scatchard plots and calculates K_d and B_{max} values as summarized in the inset table. The assays were repeated three times. Data are presented as mean ± SEM. Significant difference with p-value for each group of data was statistically analyzed by Student's t-test as indicated (n=3, $P<0.01$**, $P<0.05$*, and ns, no significance).

TvFACPα represses F-actin assembly in *T. vaginalis*

By western blotting, the anti-*Tv*FACPα antibody identified a ~30-kDa protein band in the total lysate from TH17 trophozoites (Figure 6A) and colocalized with TRITC-phalloidin with the Pearson's correlation coefficient value of 0.96, indicating the colocalization of *Tv*FACPα with F-actin in this parasite (Figure 6B). To further study if *Tv*FACPα regulates F-actin polymerization, HA-*Tv*FACPα wild type or actin-binding domain deletion mutant △237 were overexpressed in TH17 trophozoites. By IFA, HA-*Tv*FACPα was detected as network-like structures extending extensively into the cytoplasm and slightly intense immunostaining condensed near the cell membrane (Figure 6C). In the non-transgenic control TH17, α-actin was distributed in the cytoplasm as fine-dense tubular networks. However, cytoplasmic α-actin was observed as numerous stubby rods with punctate signals in HA-*Tv*FACPα-overexpressed TH17, and the pattern in △237 transfectants was similar to that in the non-transgenic TH17 control, indicating that *Tv*FACPα overexpression may alter α-actin organization in this parasite.

In western blotting, HA-*Tv*FACPα or △237 were overexpressed at a level ~5-fold higher than the endogenous form in the non-transgenic control, and the former inhibited endogenous *Tv*FACPα

333   expression in the transfectant (Figure 6D), suggesting that this parasite may have a feedback
334   mechanism to maintain cellular *Tv*FACPα levels. Western blotting showed that the expression of α-
335   actin or α-actinin did not change between transfectants (Figure 6D). Actin fractionation revealed that
336   ~45% F-actin co-sedimented with ~25% *Tv*FACPα in the non-transgenic TH17 control. In transfectants
337   overexpressing HA-*Tv*FACPα, the F-actin level reduced to ~25% but co-sedimented HA-*Tv*FACPα
338   was ~2-fold higher than the endogenous form of the non-transfectant. In the △237 mutant, the F-actin
339   ratio was slightly higher but co-sedimented △237 was lower than the non-transfectant, therefore,
340   *Tv*FACPα may repress actin polymerization. A similar trend was observed for α-actinin. By
341   immunoprecipitation, co-precipitated α-actin and α-actinin were detected in HA-*Tv*FACPα but much
342   less in the △237 mutant (Figure 6E), indicating that actin-binding activity is essential for *Tv*FACPα to
343   inhibit actin assembly.

15

Fig. 6

344
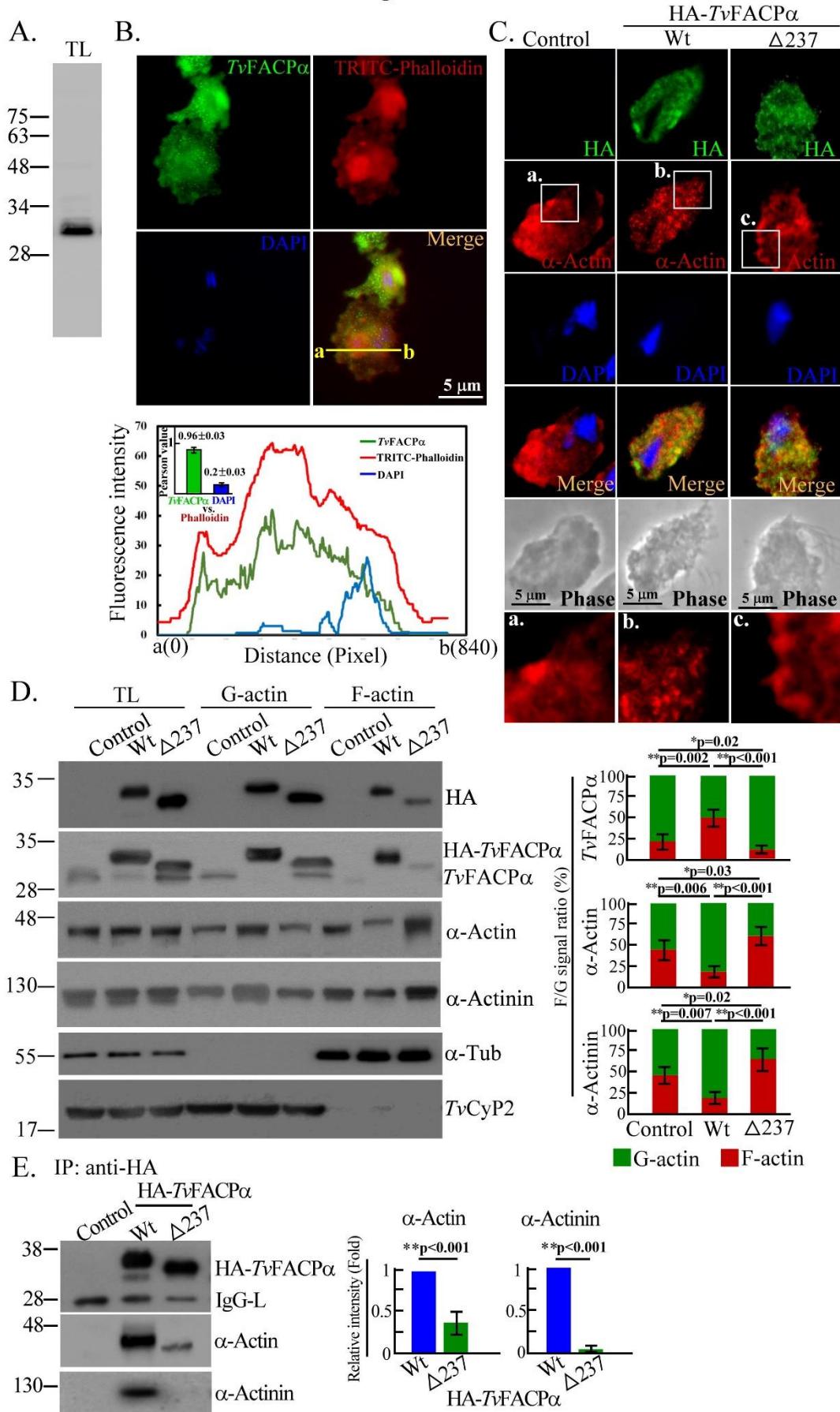
Figure 6. *Tv*FACPα binds actin to block F-actin assembly in *T. vaginalis*. (A.) The total lysate from TH17 trophozoites was subjected to western blotting with an anti-*Tv*FACPα antibody. (B.) TH17 trophozoites cultivated on a glass slide were co-stained with anti-*Tv*FACPα antibody and TRITC-Phalloidin. Signal was assessed by the plot profile analysis to display intensity distribution between sites a to b on the yellow line. The colocalization of phalloidin with α-actin or DAPI was evaluated by Pearson correlation coefficient as shown in the inset histogram. Data are presented as mean ± SEM. Scale bar: 5 μm. (C.) The IFA from the non-transgenic control and transgenic TH17 trophozoites overexpressing HA-*Tv*FACPα or △237 were detected by anti-HA and anti-α-actin. The magnified regions were boxed and images are shown in a-c. Scale bar: 5 μm. (D.) Total lysates and actin fractionations from non-transgenic control and transgenic TH17 trophozoites were examined by western blotting. The ratio of indicated protein signal in F-actin and G-actin fractions (F/G) was analyzed as shown in the histogram. (E.) The total lysates from the trophozoites as shown in (D.) were immunoprecipitated with an anti-HA antibody for western blotting. The relative intensity of indicated protein signal was measured and shown in the histogram. All assays were repeated three times. Data in histogram are presented as mean ± SEM. Statistical significance with p-value for each group of data was analyzed by Student's t-test as indicated (n=3, $P< 0.01^{**}$, $P<0.05^*$, and ns, no significance).

TvFACPα function in actin polymerization is regulated by CKII signaling.

Compared to the nonadherent T1 isolate, more *Tv*FACPα and α-actin were detected in adherent TH17 isolates but less *Tv*FACPα co-sedimented with F-actin (Figure 7-Figure Supplement 1). The immunostaining of α-actin was different between the flagellate and amoeboid forms of the adherent isolate (Figure 2B), with equal amounts of *Tv*FACPα, α-actin, and α-actinin detected in the total lysates (Figure 7A). The F-actin ratio in the amoeboid trophozoites was two-fold higher than the flagellate form (Figure 7A), whereas the *Tv*FACPα co-sedimented with F-actin in amoeboid trophozoites was two-fold lower than flagellate form. A similar trend was observed for α-actinin, indicating that adhered-amoeboid *T. vaginalis* displays more active F-actin polymerization and less *Tv*FACPα binding α-actin.

Regarding the post-translation modifications of *Tv*FACPα, *Tv*FACPα Ser[2] was previously predicted as a CKII phosphorylation sites (Figure 4D) potentially recognized by a phospho-motif (pS/pTDXE)-specific antibody, referred to as *Tv*FACP(pS2). When *Tv*FACPα was equally immunoprecipitated from the trophozoites, more *Tv*FACP(pS2) but less α-actin and α-actinin were co-pulled down from the amoeboid trophozoites than the flagellate form (Figure 7B). Ser[2] hyper-phosphorylation enriched in the amoeboid form trophozoites, in which *Tv*FACPα binding α-actin or α-actinin was low. To confirm the role of Ser[2] phosphorylation in the complex formation of *Tv*FACPα and α-actin, hypo-phosphorylation mimic S2A or hyper-phosphorylation mimic S2D mutant were introduced into TH17 trophozoites for actin fractionation and immunoprecipitation. The overall level of α-actin and α-actinin were similar in the total lysates from *Tv*FACPα, S2A, and S2D transfectants.

384   Compared to the non-transgenic control, both HA-TvFACPα and S2A overexpression repressed F-actin

385   levels in the transfectants, with higher levels of co-sedimented HA-TvFACPα or S2A in the F-actin

386   fraction (Figure 7C). By contrast, a similar level of F-actin was detected in the non-transfectant and

387   S2D mutants but co-sedimented S2D in the F-actin fraction was lower than HA-TvFACPα (Figure 7D).

388   Similar results were obtained for α-actinin. Furthermore, α-actin signals co-immunoprecipitated from

389   the S2A and S2D mutant were three-fold higher and 70% lower respectively than HA-TvFACPα

390   (Figures 7E and 7F), with the low signal intensity of α-actin co-immunoprecipitated with △237 mutant,

391   implying that Ser^2 phosphorylation is crucial for the actin-binding activity of TvFACPα. Meanwhile,

392   the low intensity of TvFACP(pS2) signal precipitated from △237 mutant implying that the actin-

393   binding domain integrity might be important for Ser^2 phosphorylation. Ser^2 phosphorylation is a major

394   signal for the dissociation of TvFACPα and α-actin. The undetectable TvFACP(pS2) signal in the S2A

395   or S2D mutant proves the antibody specificity.

396   To verify whether Ser^2 phosphorylation is regulated by CKII signaling, TH17 trophozoites

397   overexpressing HA-TvFACPα were treated with DMSO or TBB for immunoprecipitation and actin

398   fractionation, showing that the overall expression of HA-TvFACPα or α-actin was not influenced by

399   TBB treatment. When an equal amount of HA-TvFACPα was immunoprecipitated from the

400   trophozoites treated with or without TBB, decreasing TvFACP(pS2) but increasing α-actin signals were

401   detected in the co-immunoprecipitants from the parasite treated by TBB (Figure 7G). Furthermore, the

402   overall expression of TvFACPα, α-actin, and α-actinin remained constant in TH17 trophozoites with or

403   without TBB treatment, and when F-actin in TBB-treated parasite was inhibited to one-third of the

404   basal level, the TvFACPα co-sedimented with F-actin was three-fold higher than the DMSO control

405   (Figure 7H). In summary, CKII-dependent Ser^2 phosphorylation triggers dissociation of TvFACPα and

406   α-actin to evoke actin polymerization.

18

Fig. 7
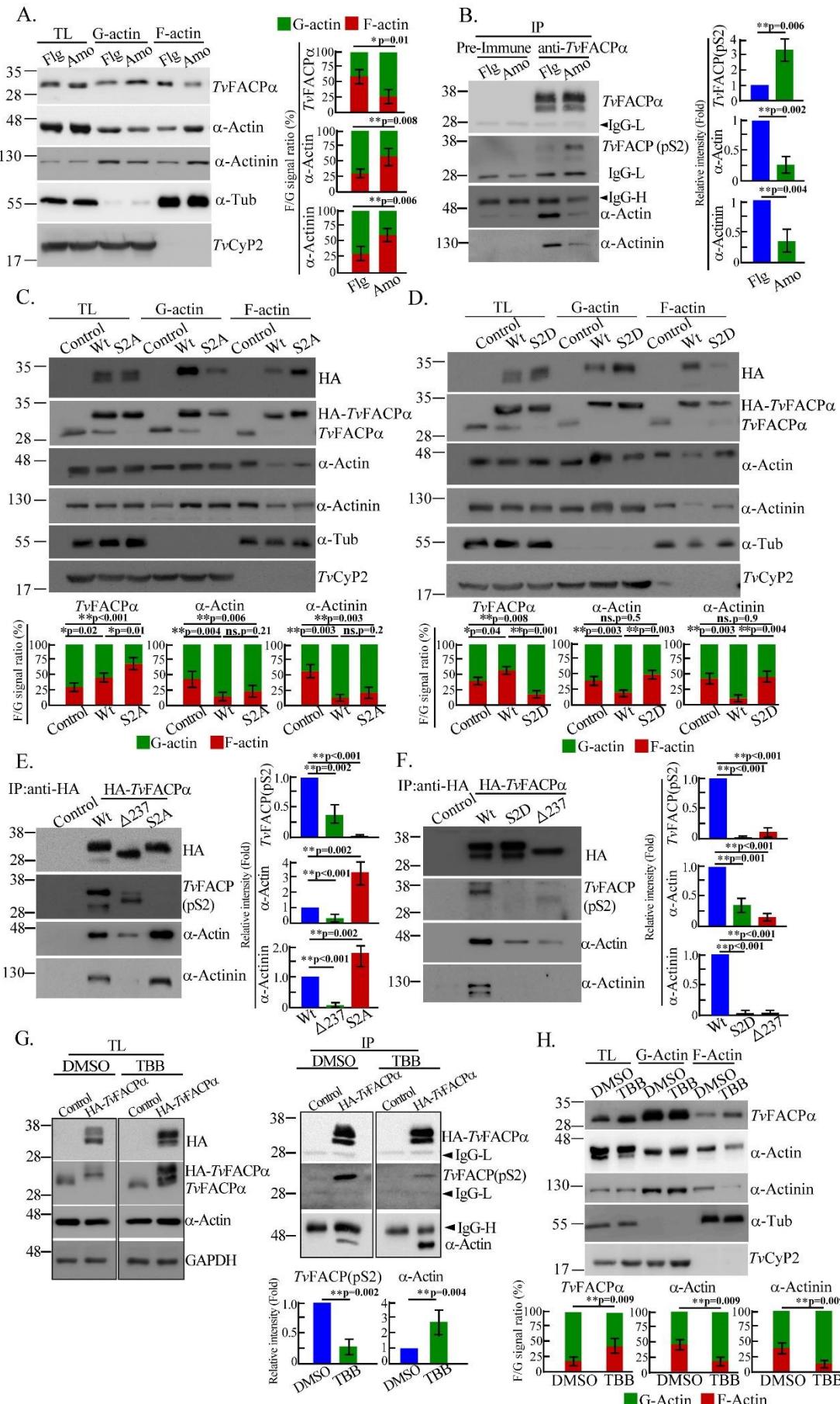
Figure 7. CKII signaling regulates actin-binding of *Tv*FACPα. (A.) Total lysates from TH17 trophozoites in the flagellate (Flg) and amoeboid (Amo) forms were fractionated to determine the ratio of indicated protein signal in F-actin to G-actin (F/G) by western blotting. (B.) The immunoprecipitants from total lysates from (A.) by anti-*Tv*FACPα antibody were examined by western blotting. (C., D.) Total lysates from the non-transgenic control or TH17 trophozoites overexpressing HA-*Tv*FACPα and S2A as shown in (C.), or S2D as shown in (D.), were fractionated for western blotting. The ratio of indicated protein signal from F-actin and G-actin fractions (F/G) was analyzed as shown in the histogram. (E., F.) The total lysates from trophozoites overexpressing HA-*Tv*FACPα and S2A as shown in (E.) or S2D as shown in (F.), were immunoprecipitated by an anti-HA antibody for western blotting. The relative intensities of indicated signals were quantified as shown in the histograms. (G.) The total lysates from the non-transgenic control or HA-*Tv*FACPα-overexpressed TH17 trophozoites with DMSO or TBB treatment were sampled for western blotting (left panel) or immunoprecipitation by anti-HA antibody (right panel). The relative intensities of signals were quantified as shown in the histogram. (H.) TH17 trophozoites treated with DMSO or TBB were fractionated for western blotting. The ratio of indicated protein signal in F-actin and G-actin fractions (F/G) was quantified as shown in the histogram. All assays were repeated three times. Data are presented as mean ± SEM. Statistical significance with p-value for each group of data was measured by Student's t-test as indicated (n=3, $P< 0.01$**, $P<0.05$**, and ns, no significance).

***Tv*FACPα in morphogenesis and cytoadherence of *T. vaginalis*.**

To examine the role of Ser^2 phosphorylation on cytoskeleton behaviors, the morphogenesis of TH17 trophozoites overexpressing HA-*Tv*FACPα and derived mutants was observed by phase-contrast microscopy. Morphogenesis in the trophozoites overexpressing HA-*Tv*FACPα and S2A was reduced to ~20% compared to ~70% morphogenesis in the non-transgenic control, whereas it was restored to ~70% in the △237 and S2D mutants (Figure 8A). TBB treatment also reduced the morphological transformation of TH17 trophozoites from ~80% in DMSO control cells to ~30% in the TBB-treated trophozoites. Notably, the TBB effect inhibiting morphogenesis was abolished in the S2D transfectant, suggesting that CKII-dependent Ser^2 phosphorylation in *Tv*FACPα is crucial to the regulation of morphogenesis in *T. vaginalis* (Figure 8B). The differential cytoadherence of various HA-*Tv*FACPα transfectants was monitored over time, showing that the non-transgenic TH17 trophozoites achieved ~100% cytoadherence 60-min post-infection, reducing to ~40% in HA-*Tv*FACPα and S2A transfectants and increasing to ~80% in △237 and S2D transfectants. TBB treatment also significantly reduced the cytoadherence 60-min post-infection and this effect was abrogated in the S2D transfectant (Figure 8D). Notably, the overexpression of HA-*Tv*FACP and related mutants or TBB treatment did not affect the cytoadherence at the initial 20-min infection (Figure 8C). These findings were consistent with our previous observation that LatB only perturbed cytoadherence from the staging 60-min post-

447 infection (Figure 3D). The data strongly supports that CKII-dependent Ser^2 phosphorylation regulates

448 *Tv*FACPα function in cytoskeleton-mediated morphogenesis and consequential cytoadherence of *T.*

449 *vaginalis*. The morphogenesis capacity of this parasite tightly correlates its cytoadherence.

Fig. 8

450

21
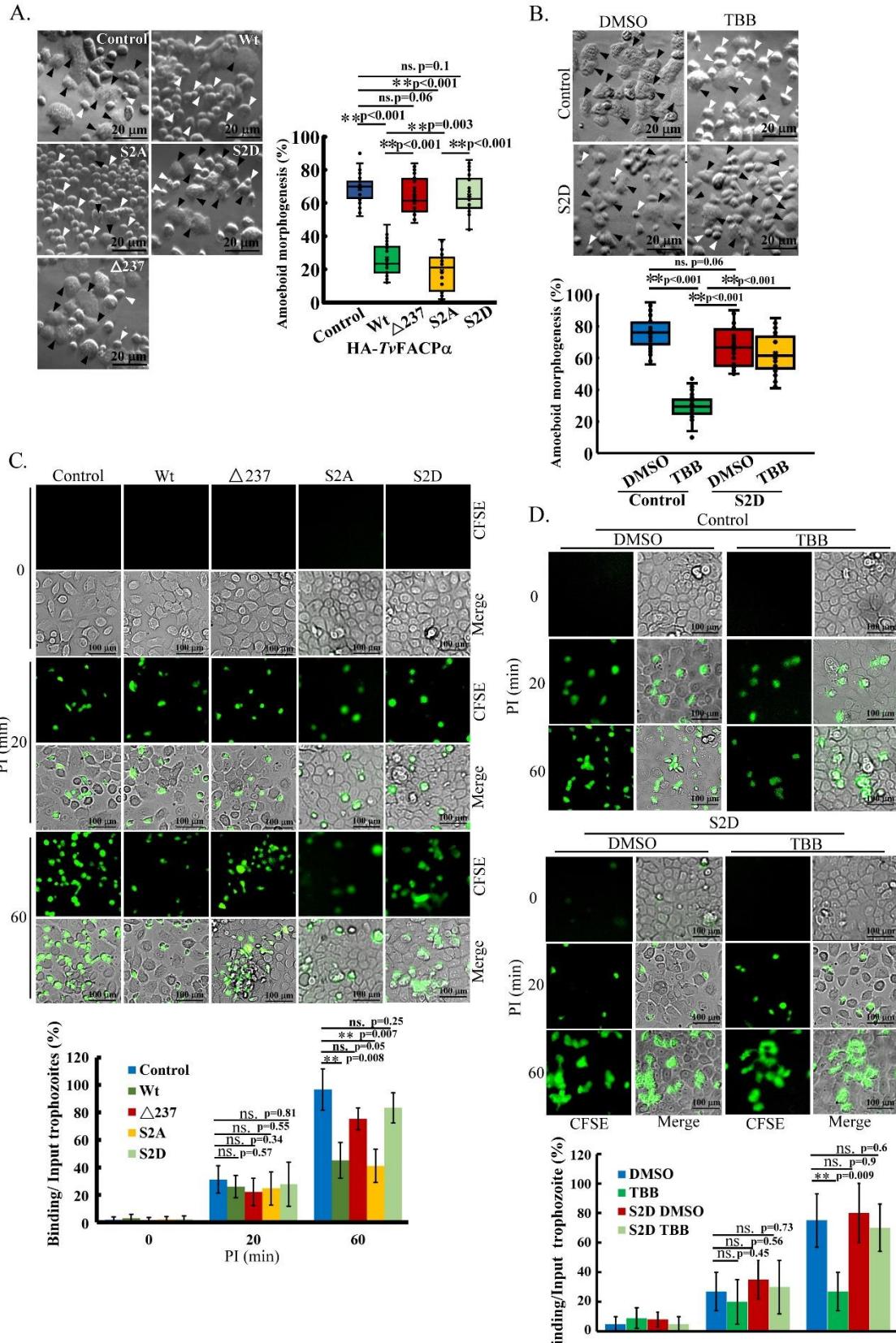
451 **Figure 8. *Tv*FACPα regulates actin-related morphogenesis and cytoadherence in *T.***
452 ***vaginalis*.** (A., B.) Non-transgenic control and transgenic TH17 trophozoites overexpressing
453 HA-*Tv*FACPα, △237, S2A, and S2D as shown in (A.), and the non-transgenic TH17
454 trophozoites and those overexpressing S2D with DMSO and TBB as shown in (B.), were
455 cultured on the glass slide for 1 hr. The cell morphology was recorded by phase-contrast
456 microscopy. The proportion of parasites in amoeboid form was measured in ~600
457 trophozoites from 12 microscopic fields as shown in the box and whisker plots. The black
458 and white arrowheads respectively indicate the representative amoeboid and flagellate forms
459 of trophozoites. Scale bar: 20 μm. (C., D.) For the cytoadherence binding assay, the CFSE-
460 labeled trophozoites overexpressing HA-*Tv*FACPα and derived mutants as shown in (C.), or
461 the non-transgenic or S2D transgenic TH17 trophozoites pretreated with DMSO and TBB as
462 shown in (D.), were co-cultured with *h*VECs for the indicated timeframes. After removing
463 unbound trophozoites, the ratios of those binding versus input was measured as shown in the
464 histograms. Scale bar: 100 μm. All assays were repeated three times. Data in histogram are
465 presented as mean ± SEM. Statistical significance with p-value for each group of data was
466 analyzed by Student's t-test as indicated (n=3, $P < 0.01$**, $P<0.05$**, and ns, no significance).

467

468

469 **The function of *Tv*FACPα in amoeboid migration.**

470 The conversion of morphology and motility is the dominant features in adherent isolates (Video
471 1) and retarded by LatB (Figure 3C), so we investigated the role of *Tv*FACPα in amoeboid migration.
472 Since cytoskeletal disorder retarded the morphogenesis and reduced the adherent activity of *T.*
473 *vaginalis*, the conditional trophozoites had to be sufficiently cultured in the T25 flask until forming a
474 confluent parasite monolayer for the wound heal assay. The wound recovery rate was significantly
475 suppressed in the TH17 trophozoites overexpressing HA-*Tv*FACPα but the rate was similar in the non-
476 transgenic control and △237 mutant, indicating that actin-binding activity is essential for *Tv*FACPα to
477 reduce the amoeboid migration (Figure 9A). Also, the wound recovery rate in the non-transgenic
478 parasite was inhibited by TBB to a similar level to the HA-*Tv*FACPα transfectant. By contrast, the
479 wound closure rate in the S2D mutant was similar to the non-transgenic parasite and not influenced by
480 TBB treatment (Figure 9B), revealing that the S2D mutant counteracted the TBB inhibitory effect on
481 amoeboid migration. This observation indicates that CKII-dependent Ser^2 phosphorylation might play
482 a key role in *Tv*FACPα-regulated amoeboid migration.

483

484 ***Tv*FACPα regulates motility switching in *T. vaginalis*.**

485 Next, we tested whether parasite motility is changed with the morphology transition using the
486 trans-well system (Figure 9C). The relative GAPDH signal in the western blotting indicates the relative
487 amount of migratory trophozoites between the bottom wells and top inserts. When GAPDH expression
488 was equal in the input trophozoites, the HA signal was also similar between the transfectants. Focusing
489 GAPDH signal from the bottom well of the 30-min trans-well plate, HA-*Tv*FACPα was higher but

490   △237 and S2D mutants were lower than the non-transgenic control, revealing that more trophozoites
491   with HA-TvFACPα overexpression migrated into the bottom well in a short time (Figure 9D). As
492   observed by microscopy, the trophozoites in the bottom well displayed the morphology at the free-
493   swimming flagellate form (Figure 9-Figure Supplement 1), suggesting that HA-TvFACPα
494   overexpression may retain the parasite in the flagellate form with faster movement driven by motile
495   flagellum. The motility conversion involved actin binding activity regulated by Ser^2 phosphorylation.
496   TBB inhibited Ser^2 phosphorylation in TvFACPα (Figure 7G), with the GAPDH signal from the TBB-
497   treated trophozoites in the bottom well higher than in the DMSO-treated trophozoites (Figure 9D).
498   Together, TvFACPα Ser^2 hypo-phosphorylation retarded amoeboid migration in the adhered
499   trophozoites but expanded the population of free trophozoites that rapidly moved via flagellar
500   locomotion (Figure 9E).

Fig. 9

501
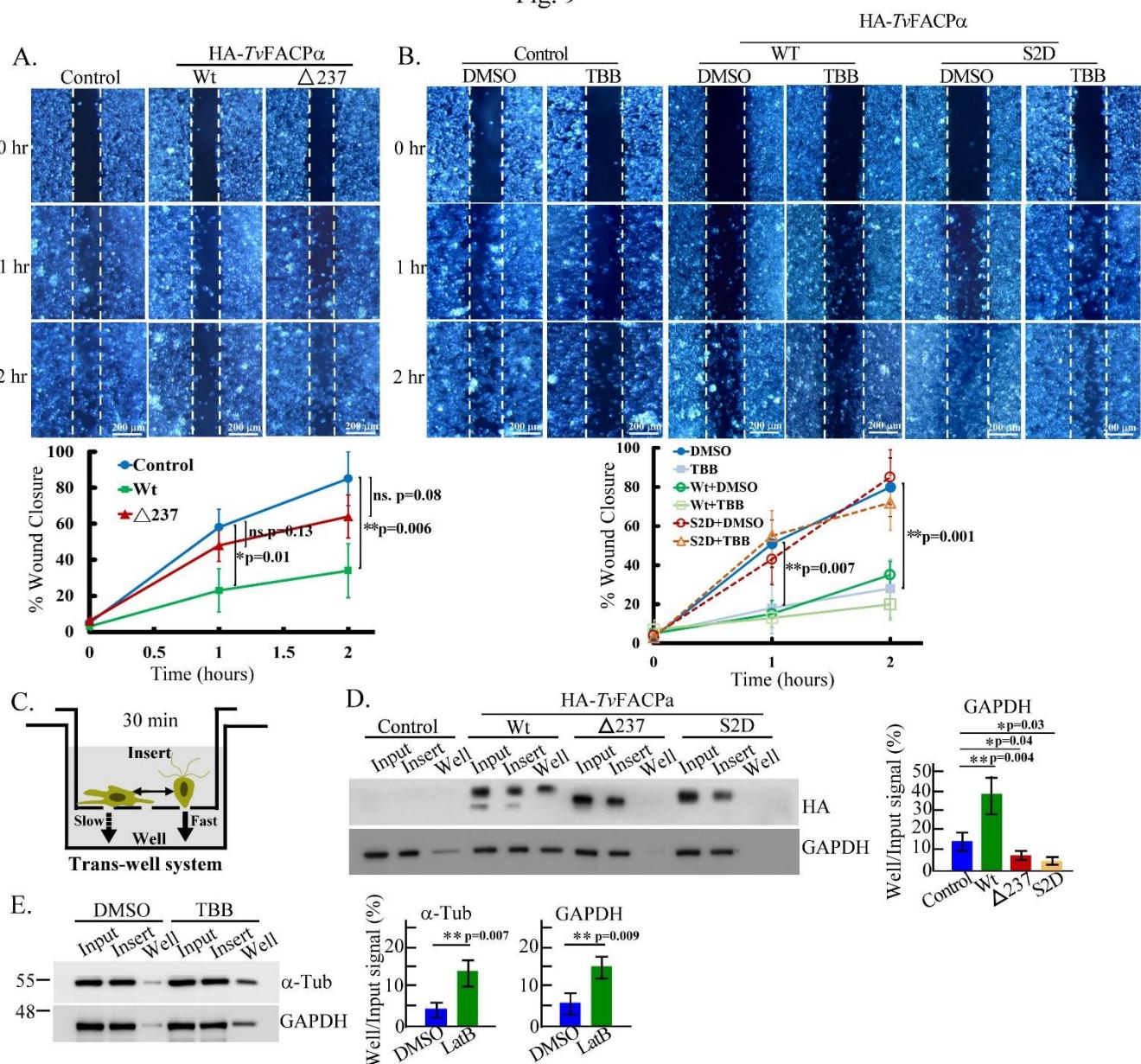
Figure 9. TvFACPα regulates ameboid migration and motility switching of *T. vaginalis*.

503   (A., B.) The migrations of non-transgenic control and TH17 trophozoites overexpressing HA-
504   *Tv*FACPα and △237 in (A.), those overexpressing HA-*Tv*FACPα and S2D with DMSO or
505   TBB treatment in (B.), were evaluated by a scratch wound healing assay. The representative
506   images showing wound closure were captured at 0, 1, and 2 hr, and the closure rate was
507   measured by the percentage of wound recovery area at indicated time points as shown in the
508   line charts. The white dash lines mark the wound scratched boundaries. Scale bar: 200 μm.
509   (C.) A schematic diagram illustrates the working principle of a trans-well system applied to
510   assess migration. Within a short interval, the free trophozoites swim by flagellar locomotion
511   to pass through the boundary membrane faster than crawling by pseudopodia migration. (D.,
512   E.) The migrations of TH17 trophozoites overexpressing HA-*Tv*FACPα, △237, and S2D in
513   (D.), TH17 trophozoites treated with DMSO and TBB in (E.), were evaluated by trans-well
514   assay. The relative intensities of signals in the bottom well were evaluated by western blotting
515   and quantified as shown in the histograms. All assays were repeated three times. Data are
516   presented as mean ± SEM. Statistical significance with p-value for each group of data was
517   statistically measured by Student's t-test as indicated (n=3, $P< 0.01$**, $P<0.05$**, and ns, no
518   significance).

519
520

Discussion

522   *Tv*FACPα was identified as an actin-binding protein that suppressed actin polymerization via the
523   direct interaction with G-actin monomers and F-actin polymers. Furthermore, CKII-dependent
524   signaling plays a key in the switch from morphology and motility. These cytoskeleton-mediated
525   behaviors are crucial for optimizing the cytoadherence and population spread of this parasite. In the
526   human urogenital tract, the intermittent flushing action of body fluid generates a mechanical barrier to
527   either impair or eliminate the retention of uropathogenic microbes, therefore switching to the opportune
528   motility mode to instantly counteract the environmental challenges or physical defenses would be
529   beneficial for *T. vaginalis* colonization (37).

530   Unfortunately, the real-time tracking system for fluorescence protein within a living parasite did
531   not work in our assay system, so the overall actin assembly and cytoskeleton activities were evaluated
532   by western blotting and IFA to show the relevance of *Tv*FACPα and actin dynamics in the adherent
533   trophozoites under a steady-state condition.

534   The DNA sequences of the *tvfacpα* gene from nonadherent and adherent *T. vaginalis* isolates share
535   100% identity (38), thus the differential cytoskeleton behaviors between isolates are unlikely to be
536   attributed to sequence polymorphism in *Tv*FACPα. Meanwhile, α-actin overexpression dose not
537   promote adherence in the nonadherent isolate, thus cytoskeleton-dependent cytoadherence is unlikely
538   to be determined by one single molecule.

539   Compared to the nonadherent T1 isolate, more *Tv*FACPα and α-actin were detected in adherent
540   TH17 isolates but less *Tv*FACPα co-sedimented with F-actin (Figure 7-Figure Supplement 1), possibly
541   explaining why the adherent isolate displays more active cytoskeleton behaviors than the nonadherent

isolate. Furthermore, the adherent isolate may require a larger TvFACPα reservoir to immediately modulate cytoskeleton dynamics in response to sudden environmental challenges.

The perinuclear actin cap was observed in the trophozoite with dividing nuclei. One of the known functions of the perinuclear actin cap is to govern nuclear location and movement during nuclear division (39), therefore F-actin may function in the nuclear division of this parasite. When there was colocalization of TvFACPα and F-actin at the leading edge of the extending pseudopodia, there was less colocalization observed near the actin cap (Figure 6), suggesting that F-actin bundle assembly in peripheral motile structure is presumably manipulated by TvFACPα, distinct from that in the central juxtanuclear actin cap. Human CKIP-1 protein containing pleckstrin homology domain directs CPα to the cell membrane periphery and bridges the interaction of CPα with CKII kinase to co-regulate cell morphology (33, 34).

TvFACPα Ser^2 identified as a CKII phosphorylation site is conserved with Ser^9 on human or yeast CPα (Figure 4D) (33, 34, 40). Human CPα Ser^9 has been demonstrated to be phosphorylated by CKII kinase but does not directly affect actin assembly (33), indicating that the regulation of human CPα is divergent to TvFACPα in this early evolutionary-branched protozoan. Also, yeast CPα Ser^9 resides in the stalk domain but not the actin-binding domain, thus Ser^2 phosphorylation may not directly interfere with TvFACPα actin-binding, instead altering function by an allosteric effect or binding with other CPα interacting partners to co-regulate actin dynamics (40).

Iron was previously found to trigger a protein kinase A-dependent signaling to activate the Myb3 transcription factor sequential phosphorylation and ubiquitination essential to its nuclear translocation (48). However, iron was observed to slightly change *T. vaginalis* morphogenesis long-term cultured in iron-restricted growth medium, so whether iron triggers the CKII pathway to regulate cytoskeleton dynamics in this parasite remains to be elucidated.

When the gain- or loss-of-function assay was employed to study the role of Ser^2 phosphorylation, F-actin assembly was repressed in the hypo-phosphorylation mimic S2A mutant but restored to near the basal level instead of exceeding it in the hyper-phosphorylation mimic S2D mutant. This implies the existence of additional pathways promoting F-actin assembly under our tested conditions. For example, TvFim1 protein reveals an opposite function to TvFACPα to accelerate F-actin polymerization that favors phagocytosis and migration in *T. vaginalis* (35). In TrichDB database, BLAST analysis identified two CPα homologous proteins (TVAG_470230 and TVAG_212270) with 32% sequence similarity (Figure 4-Figure Supplement 2) but whether they are functionally redundant in this parasite remains to be studied.

A previous proteomic study reported that surface fibronectin-binding might change actin expression in this parasite. In this report, α-actin expression was constant in the free-swimming flagellate or adhered-amoeboid forms, implying less involvement of fibronectin-binding in the morphogenesis and cytoadherence under our test condition (15).

Mass spectrometry data revealed GAPDH as a major interacting partner of Tvactin. In chicken neuron cells, GAPDH acts as a chaperone for α-actin and co-translocates with α-actin to specialized axon sites for polymerization (41). In yeast, GAPDH associates with α-actin and RpB7 subunit of RNA

581 polymerase II to regulate transcription (42, 43). The significance of GAPDH complexed with the actin

582 cytoskeleton in *T. vaginalis* remains to be studied.

583   The EC_{50} of TBB is varied in different cell types. Numerous CKII alpha subunit (CKIIα) proteins

584 predicted from TrichDB shared less sequence consensus in the TBB binding pocket to high eukaryotic

585 CKIIα (38, 44), possibly explaining why Ser^2 phosphorylation and downstream cytoskeleton activities

586 were partially inhibited by TBB treatment. Again, the S2D mutation was unable to promote actin

587 polymerization efficiency beyond that of the non-transgenic parasite, suggesting that actin filament

588 growth might be modulated by additional pathways.

589   The opportunistic amoeba, *Naegleria fowleri,* exists in three life stages: flagellate trophozoite,

590 amoeba trophozoite, and cyst. Multiple environmental factors, like growth temperature, cation level,

591 steroid hormone, or chemical agents, affect the flagellate to amoeba transformation (45, 46, 47). In *T.*

592 *vaginalis*, other than the contact-dependent effect (14, 18, 35), the factors that trigger the morphological

593 transition are virtually unknown. Overexpression of actin increases the phagocytosis and cytotoxicity

594 of *N. fowleri* (20) but does not affect *T. vaginalis.* (Figure 2-Figure Supplement 1). Although they have

595 the cognate behavior of flagellate-amoeba conversion, their regulation in these two protozoa is distinct.

596 The immediate conversion to motility may allow the parasite to rapidly respond to environmental

597 fluctuations or flushing by humoral fluid flow in the urogenital tract (37).

598   LatB had little effect on the initial 20-min cytoadherence and surface expression of adhesion

599 molecules, AP, PFO, and cadherin, thus we speculate that the adhesion molecules on the cell surface

600 may play roles in the initial cytoadherence, thereafter actin-based morphogenesis reinforces

601 cytoadherence at the later stage of cytoadherence (49). In our previous study, *Tv*CyP2 was

602 demonstrated to shuttle between intracellular membrane compartments, involving the endoplasmic

603 reticulum, Golgi apparatus, and hydrogenosome before translocation onto the cell membrane (50). The

604 cell surface presentation of adhesion proteins may occur through similar endomembrane trafficking

605 routes.

606

Conclusion

608   In conclusion, *Tv*FACPα directly binds G- or F-actin to block actin filament extension (Figure

609 10), with Ser^2 phosphorylation on *Tv*FACPα decreasing actin-binding activity and triggering actin

610 polymerization. In adherent *T. vaginalis* trophozoites, *Tv*FACPα spatially colocalizes with actin

611 molecules at the membrane periphery of motile protrusive pseudopodia, where *Tv*FACPα regulates

612 actin assembly dynamics to control the cytoskeleton behaviors of motility switching, amoeboid

613 migration, or cytoadherence consequent to the morphogenesis. The Ser^2 phosphorylation status is

614 crucial for *Tv*FACPα function in the regulation of cytoskeleton behaviors. The cytoskeleton-driven

615 activities are also inhibited by a cytoskeleton (LatB) or CKII (TBB) inhibitor. These findings may

616 provide potential therapeutic targets for cytoskeleton aspects to prevent *T. vaginalis* colonization and

617 transmission.

Fig. 10
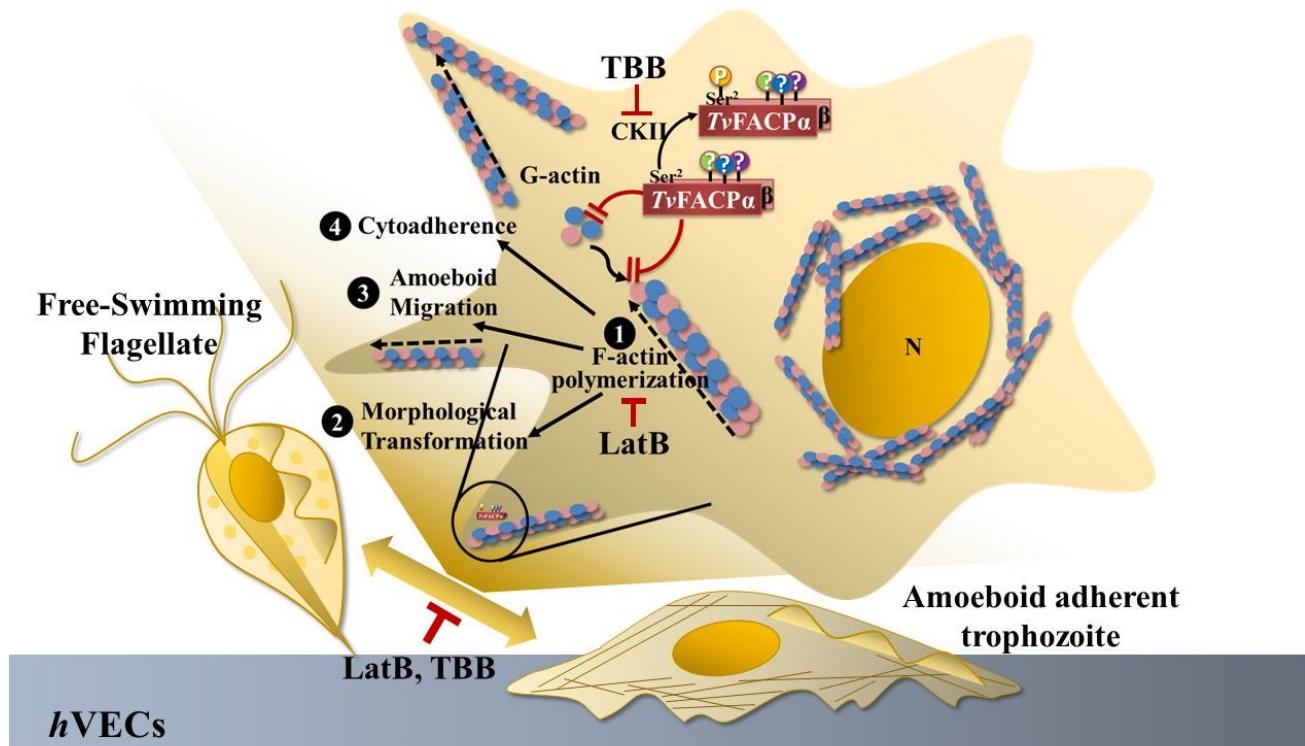
Figure 10. The proposed model for *Tv*FACPα function and regulation. *Tv*FACPα is an actin-binding protein containing a c-terminal actin-binding domain and CKII-dependent Ser^2 phosphorylation. *Tv*FACPα directly interacts with G-actin and F-actin through the actin-binding domain, and Ser^2 phosphorylation is the essential signal triggering dissociation of *Tv*FACPα and α-actin. *Tv*FACPα colocalizes with actin at the leading edge of the peripheral motile protrusions inhibiting actin filament polymerization ❶, leading to the diminishment of the flagellate-amoeboid transformation and motility switching ❷, amoeboid migration❸, and the cytoadherence ❹ in this parasite. As expected, the above behaviors were also inhibited by TBB and LatB, supporting the significance of CKII and cytoskeleton activities on parasitism. Tight adherence and immediate migration conversion may be approaches adopted by this parasite to counteract environmental fluctuations or evade the host defense. This novel mechanism of *T. vaginalis* cytoadherence may provide new therapeutic targets for future treatment.

Materials and Methods

Cell cultures

T. vaginalis trophozoites were cultured in TYI medium at 37℃ (48). Two *T. vaginalis* isolates, nonadherent T1 (48) and adherent TH17, were used in this study. T1 with only flagellate trophozoites freely swim in the medium suspension. TH17 displayed vigorous morphogenesis and tightly adhered

27

639 on glass surface of culture tube. Once the void surface is saturated by adhered trophozoites, the
640 unbound parasite at the flagellate form freely swims in the medium suspension (Figure 1 and Videos 1
641 and 2). The flagellate trophozoites in the medium suspension and adherent trophozoite on the culture
642 tube surface were collected for analysis as described below. Human vaginal epithelium cells (hVECs,
643 VK2/E6E7) were cultivated in Keratinocyte-Serum Free medium (Thermo Fisher Scientific,
644 Massachusetts, USA) at 37°C in 5% CO_2 as the suggestion by ATCC.

645

Lysate preparation from adherent-amoeboid and nonadherent-flagellate trophozoites.

647 Approximately 2×10^7 trophozoites from TH17 adherent isolate were inoculated into culture tube
648 with 15 ml of medium and incubated at 37°C for 2 hr. The free-trophozoites in suspension were
649 transferred to a new tube and recovered by centrifugation. The cell pellet was lysed in 1 ml lysis buffer
650 (1% Triton X-100, 1× Protease inhibitor cocktail, 1×Phophatase inhibitor cocktail, 100 μg ml^{-1} TLCK,
651 5 mM EDTA, in TBS). The trophozoites adhering to the glass tube were directly lysed by adding 1 ml
652 lysis buffer and vigorously vortexing for 5 min at 4°C.

653

Plasmid construction

655 The full-length coding sequence of the *tvfacpα* gene (TVAG_470230) was amplified from *T.
656 vaginalis* genomic DNA using the primer pair of *Tv*FACPα-BamHI-5′ and *Tv*FACPα-XhoI-3′. The PCR
657 product was gel-purified, then digested by BamHI/XhoI, and ligated into BamHI/XhoI-predigested
658 Flp-HA-*Tv*CyP2 or pET28a backbone plasmid to obtain Flp-HA-*Tv*FACPα or pET28-His-*Tv*FACPα
659 plasmid. Following a similar procedure, the DNA fragments were amplified from Flp-HA-*Tv*FACPα
660 individually using the primer pairs, *Tv*FACPαS2A-5′ and *Tv*FACPα-XhoI-3′ for the S2A mutation,
661 *Tv*FACPαS2D-5′ and *Tv*FACPα-XhoI-3′ for the S2D mutation, and *Tv*FACPα-BamHI-5′ and
662 *Tv*FACPα△237-3′ for the actin-binding domain deletion mutant (△237). The PCR products were gel-
663 purified and subcloned into Flp-HA-*Tv*FACPα or pET28a backbone with BamHI/XhoI sites to generate
664 Flp-HA-*Tv*FACPα(S2A), Flp-HA-*Tv*FACPα(S2D), Flp-HA-*Tv*FACPα(△237), or pET28-His-
665 *Tv*FACPα(△237) plasmid.

666 To express HA-tagged α-actin in *T. vaginalis* or glutathione S-transferase (GST) fused-α-actin
667 for the GST pull-down or actin polymerization assays, the full-length coding sequence of the *tvactin*
668 gene (TVAG_337240) was amplified from *T. vaginalis* genomic DNA by the primer pair of *Tv*actin-
669 BamHI-5′ and *Tv*actin-XhoI-3′. The gel-purified PCR product was digested with BamHI and XhoI,
670 then ligated into BamHI and XhoI-predigested Flp-HA-*Tv*FACPα or pGST-*Tv*CyP2 plasmid (50) to
671 generate Flp-HA-*Tv*actin, or pGST-*Tv*actin plasmid.

672 The *Tv*Cadherin expression plasmid was constructed, the coding sequence of the *tvcadherin* gene
673 (TVAG_393390) (2) was amplified from *T. vaginalis* genomic DNA by the primer pair of *Tv*Cadherin-
674 BamHI-5′ and *Tv*Cadherin-XhoI-3′, and subcloned into Flp-HA-*Tv*FACPα backbone vector with
675 *BamH*I and *Xho*I sites to produce Flp-HA-*Tv*Cadherin plasmid.

676

677

678   The primer oligonucleotides used in this study.

Primer	Sequence
*Tv*FACPα-BamHI-5′	(5′AA<u>GGATCC</u>ATGAGCGAGAGCGAAAAT3′)
*Tv*FACPα-XhoI-3′	(5′AA<u>CTCGAG</u>TTAGCACTTCATGCCACC3′)
*Tv*FACPα△237-3′	(5′AA<u>CTCGAG</u>ACGAAGCTGGAAAAGAAC3′)
*Tv*FACPαS2A-5′	(5′AA<u>GGATCC</u>ATG*gcc*GAGAGCGAAAATATC3′)
*Tv*FACPαS2D-5′	(5′AA<u>GGATCC</u>ATG*gat*GAGAGCGAAAATAT3′)
*Tv*actin-BamHI-5′	(5′AA<u>GGATCC</u>ATGGCTGAAGAAGACGTTCAGAC3′)
*Tv*actin-XhoI-3′	(5′AA<u>CTCGAG</u>TTAGAAGCACTTGCGGTGGAC3′)
*Tv*Cadherin-BamHI-5′	(5′<u>GGATCC</u>ATGATTTGGACTTTTTTATTGCAG3′)
*Tv*Cadherin-XhoI-3′	(5′<u>CTCGAG</u>TTACTTTCTAAGCCAAAGAATTATTACT-3′)

690   The restriction sites are underlined, and mutation sites are indicated in lowercase italics.

691

Cytoadherence binding assay

693   *h*VECs was cultured in a 24-well plate to an 85% confluent monolayer. Mid-log phase *T. vaginalis*

694   prelabeled with 5 μM of carboxyfluorescein diacetate succinimidyl ester dye (CFSE; CellTrace™,

695   Thermo Fisher Scientific, Massachusetts, USA), were inoculated by a multiplicity of infection (MOI)

696   of 2:1 into *h*VECs culture. At the specific time point, the medium was aspirated and unbound

697   trophozoites were removed by washing two times with PBS for 5 min each. Samples were fixed in 4%

698   formaldehyde for fluorescence microscopy.

699

Real-time microscopy

701   The activity of trophozoites on the confluent *h*VECs monolayer in a glass-bottom culture dish was

702   monitored in real-time by confocal microscopy (LSM-700, Zeiss, Oberkochen, Germany) under a

703   phase-contrast mode with the sampling rate at one frame per 15 sec over time as indicated.

704

Inhibitor treatment

706   1 μM of LatB (Sigma-Aldrich, Massachusetts, USA) or 250 μM of TBB (Sigma-Aldrich,

707   Massachusetts, USA) was added into the *T. vaginalis* culture and incubated at 37℃ for 2 hr before

708   analysis.

709

Morphology analysis

711   Trophozoites were cultured on a glass slide in a humid chamber at 37℃ for 1 hr and the

712   morphology was observed by phase-contrast microscopy (CKX31, Olympus, Tokyo, Japan). The

713   percentage of flagellate or amoeboid form was measured from 600 trophozoites within 12 random

714   microscopic fields.

715

Immunofluorescence assay (IFA)

717   *T. vaginalis* was fixed with 4% formaldehyde and permeabilized with 0.2% Triton X-100. The
718   samples were then incubated with the primary antibodies: rabbit anti-α-actin (200×, GenScript, New
719   Jersey, USA), mouse anti-α-actin (400×, Abcam Ac-40, Cambridge, UK), mouse anti-HA (200×,
720   Sigma-Aldrich HA-7, Massachusetts, USA), mouse anti-AP65 (7), rabbit anti-PFO (10), rabbit anti-
721   *Tv*FACPα, followed by reaction with FITC or Cy3-conjugated goat anti-mouse or rabbit IgG secondary
722   antibodies (200×, Jackson ImmunoResearch, Pennsylvania, USA). The specimens were air-dried and
723   mounted in medium with DAPI (Vector laboratories, California, USA) for observation by confocal
724   microscopy (LSM-700, Zeiss, Oberkochen, Germany).

725

F-actin staining

727   Trophozoites were fixed with 4% formaldehyde, then permeabilized with 0.2% Triton X-100. The
728   sample was incubated with 20 μg ml^{-1} of TRITC-conjugated Phalloidin (Sigma-Aldrich, Massachusetts,
729   USA) diluted in PBS with 1% BSA in the dark at room temperature for 1 hr. After washing three times
730   with PBS, the glass slide was air-dried and mounted in anti-fade medium (Vector laboratories,
731   California, USA) for fluorescence microscopy (BX-60, Olympus, Tokyo, Japan).

732

Signal colocalization evaluation

734   The fluorescent intensity distributed in the fluorescence assays was measured by plot analysis of
735   ImageJ (Version 1.53q, National Institutes of Health, Maryland, USA). Pearson's correlation
736   coefficient was calculated to evaluate the signal co-localization, with a value of 1 indicating perfect
737   colocalization, -1 indicating anti-correlation, and 0 representing no correlation.

738

Western blotting

740   The protein samples denatured in 1x SDS sample buffer were separated by sodium dodecyl sulfate-
741   polyacrylamide gel electrophoresis (SDS PAGE) in a 12% gel before blotted to polyvinylidene
742   difluoride (PVDF) membrane by the wet transblot system (Bio-Rad, California, USA). The blocked
743   membrane was incubated with the primary antibodies: mouse anti-HA (2,000×, Sigma-Aldrich HA-7,
744   Massachusetts, USA), mouse anti-α-actin (20,000×, Abcam Ac-40, Cambridge, UK), mouse anti-
745   *Tv*CyP2 (5,000×) (50), mouse anti-α-tubulin (10,000×, Sigma-Aldrich DM-1A, Massachusetts, USA),
746   rabbit anti-*Tv*FACPα (3,000×), mouse anti-6×His (2,000×, Abcam AD1.1.10, Cambridge, UK),
747   rabbit anti-phospho-CKII substrate [(pS/pT)DXE] (1,000×, Cell Signaling Technology, Massachusetts,
748   USA), rabbit anti-PFO (5,000×) (10), mouse anti-AP65 (10,000×) (7), mouse anti-GAPDH (10,000×)
749   (51) and mouse anti-α-actinin (5,000×) (51) at 4℃ overnight, followed by HRP-conjugated anti-
750   mouse or rabbit IgG secondary antibodies (5,000×, Jackson ImmunoReaearch, Pennsylvania, USA)
751   at 37℃ for 1 hr. The membrane reacted with the enhanced chemiluminescence substrate (ECL, Thermo
752   Fisher Scientific, Massachusetts, USA) were detected and quantified by UVP image system
753   (ChemiDoc-It 815 Imager, VisionWorksLS 8.6 software, Analytik Jena Company, Jena, Germany).

754

Immunoprecipitation

756   Briefly, 6×10^7 trophozoites were lysed in 1ml of lysis buffer (1% Triton X-100, 1× Protease

757   inhibitor cocktail, 1×Phophatase inhibitor cocktail, 100 µg ml^{-1} TLCK, 5 mM EDTA, in TBS) and

758   centrifuged to remove unbroken cell debris, before the addition of 20 µl of anti-HA antibody-

759   conjugated agarose beads (Sigma-Aldrich, Massachusetts, USA), then incubated on a rotator at 4℃

760   overnight. The beads were recovered by centrifugation and washed three times with 1ml lysis buffer.

761   The precipitates were denatured in 1× SDS sample buffer for western blotting or staining (48, 50).

762

763   **Label-free quantitative proteomic analysis**

764   The proteins separated by SDS-PAGE were fixed in methanol for SYPRO Ruby staining (Thermo

765   Fisher Scientific, Massachusetts, USA) and visualization by the Typhoon9410 imaging system (GE

766   healthcare, Illinois, USA). Each gel lane was equally cut into 4 pieces, then sliced into smaller 1-mm^3

767   cubes. The gel cubes were desalted by five washes sequentially in 1 ml of 20 mM triethylammonium

768   bicarbonate buffer (TEABC) and 1 ml of 20 mM TEABC with 50% acetonitrile, with the vigorous

769   vortex. The samples were sequentially reduced in 20 mM dithiothreitol (DTT) at 56℃ for 1 hr,

770   alkylated in 55 mM iodoacetamide in the dark at room temperature for 30 min and digested with trypsin

771   (Promega, Wisconsin, USA) at 37℃ overnight. The tryptic peptides were extracted by vortexing three

772   times sequentially in 20%, 50%, and 100% acetonitrile, then dried in a vacuum concentrator (SpeedVac,

773   Thermo Fisher Scientific, Massachusetts, USA) for LC-MS/MS analysis (48). The protein abundance

774   from the mass spectrometry data was analyzed by a label-free quantitative method by Mascot search,

775   which provides an automated calculation of the Exponentially Modified Protein Abundance Index

776   (emPAI) to estimate the coverage of the identified peptides and abundance for each protein in a dataset.

777   The identified proteins with an emPAI above 0.25 or specific in the co-pull-down sample with their

778   function category are summarized in Table 1. The mass spectrometry proteomics raw data have been

779   deposited to Dryad (https://datadryad.org/stash/share/e30mZQElM-nBNmJOniuiGSBJWBkB7V4-

780   t0XzQ891cX8) or the ProteomeXchange Consortium via the PRIDE (www.ebi.ac.uk/pride/) (52)

781   partner repository with a dataset identifier number of PXD034359.

782   PRIDE Reviewer access account details:

783   Username: reviewer_pxd034359@ebi.ac.uk, Password: XpCqEnqW

784

785   **In silico analysis of protein sequence and function**

786   The functions of the proteins identified by mass spectrometry were categorized by Protein Analysis

787   Through Evolutionary Relationships (PANTHER) Classification System (www.pantherdb.org/). The

788   *Tv*FACPα protein homologue was searched in TrichDB (trichdb.org/trichdb/app). The multiple protein

789   sequence alignment was analyzed by the Vector NTI AdvanceR 11.5.1 software (Thermo Fisher

790   Scientific, Massachusetts, USA). The protein search was performed by the Basic Local Alignment

791   Search Tool (BLAST, blast.ncbi.nlm.nih.gov/Blast.cgi) or UniProt (www.uniprot.org/).

792

793   **Production of recombinant protein**

794   The recombinant protein was produced as previously described (48, 50). The majority of GST-

795   *Tv*actin was expressed in the inclusion bodies of *E. coli* (BL21). For the GST-pull-down assay, the

796   inclusion bodies from 200 ml of *E. coli* culture were dissolved in 1 ml of 8 M urea at 4°C for 20 min

797   to solubilize the proteins. Then, 1 ml of lysate was immediately added to 14 ml PBS and incubated at

798   4°C for 30 min to refold proteins. After the removal of the insoluble pellets by low-speed centrifugation

799   at $23,000 \times g$, soluble GST-*Tv*actin was incubated with glutathione-conjugated sepharose beads as

800   suggested by the supplier (GE healthcare, Illinois, USA) at 4°C for 3 hr and then eluted in GST elution

801   buffer (50 mM Tris-HCl, 10 mM reduced glutathione, pH 8.0). For the solid-phase binding and *in vitro*

802   actin polymerization assays, the bacterial inclusion bodies were solubilized in 8 M urea and directly

803   reconstituted in 14 ml of G-buffer (0.2 mM $CaCl_2$, 0.2 mM ATP, 0.5 mM DTT, 5 mM Tris-HCl pH

804   8.0) at 4°C overnight. The insoluble materials were removed by ultracentrifugation at $100,000 \times g$ to

805   recover the soluble G-actin in the supernatant (53). Soluble G-actin was further purified by glutathione-

806   conjugated sepharose beads and eluted in G-buffer with 10 mM reduced glutathione.

807

808   **GST pull-down assay**

809   GST pull down assay was performed as previously described (50). Briefly, 80 picomoles of GST

810   or GST-*Tv*actin immobilized on 20 μl of glutathione conjugated-sepharose beads 4B (GE healthcare,

811   Illinois, USA) was incubated with 80 picomoles of His-*Tv*FACPα or derived mutants in 1 ml GST

812   binding buffer (PBS contains 0.2% Triton X-100 and 1 mM EDTA) at 4°C rotation overnight The GST

813   beads were washed three times by 1 ml of GST binding buffer then denatured in 1× SDS sample buffer

814   for further analysis.

815

816   ***Tv*FACPα antiserum production**

817   The recombinant His-*Tv*FACPα full-length protein was produced and purified by a standard

818   protocol as suggested by the supplier (QIAGEN, Hilden, Germany) (48, 50). Using the purified His-

819   *Tv*FACPα protein to immunize rabbits for antiserum production is a customized service provided by

820   the manufacturer (Genetex, California, USA). The antibody specificity of anti-*Tv*FACPα was tested by

821   western blotting as shown in Figure 6A.

822

823   ***In vitro* actin polymerization and co-sedimentation assay**

824   Insoluble GST-*Tv*actin denatured in 0.5 ml of 8M urea was reconstituted in 7.5 ml of G-buffer (0.2

825   mM $CaCl_2$, 0.2 mM ATP, 0.5 mM DTT, 5 mM Tris-HCl, pH 8.0) at 4°C overnight to ensure that the

826   thorough GST-*Tv*actin depolymerizes into the G-actin form. Then, 80 picomoles of G-actin in 1 ml of

827   G-buffer were added 1/10 volume of $10 \times$ F-buffer (500 mM KCl, 20 mM $MgCl_2$, and 10 mM ATP,

828   100 mM Tris, pH 7.5) at 4°C for 1 hr to trigger actin polymerization. F-actin was recovered from the

829   pellet by $100,000 \times g$ ultracentrifugation, whereas soluble G-actin in the supernatant (54). The ratio of

830   F-actin versus G-actin was evaluated with Coomassie blue staining or Western Blot detection.

831   Alternatively, F-actin and co-sediments were recovered from the pellet by $100,000 \times g$

832   ultracentrifugation of the *in vitro* actin polymerization assay in the presence of 80 picomoles of His-

833   *Tv*FACPα wild type or His-$\triangle$237 at 4°C for 1 hr.

834

ELISA-based solid-phase binding assay

835

836 The solid-phase binding assay was performed as described previously, with a few modifications

837 (54). Briefly, 100 μl of 2.5 μM G-actin in G-buffer or F-actin in F-buffer was added to a 96-well

838 microplate and incubated at 4℃ with gentle shaking for 8 hr. After three washes with PBST (0.05%

839 Tween 20 in PBS), the samples were blocked in PBST with 5% non-fat milk at 37℃ for 2 hr before

840 100 μl aliquots of different concentrations of His-TvFACPα (0, 2.5, 5,10, 20, 40, and 80 μM) were

841 added to the wells and incubated at 4℃ with gentle agitation overnight for protein-protein interaction.

842 Unbound protein was removed by three washes with PBST and the plate was incubated with mouse

843 anti-6×His primary antibody (10,000×, in PBST containing 5% non-fat milk) at room temperature for

844 2 hr, followed by three washes with PBST. The wells were incubated with HRP-conjugated goat anti-

845 mouse IgG secondary antibody (5000× in PBST containing 5% non-fat milk, Jackson

846 ImmunoReaearch, Pennsylvania, USA) at room temperature for 2 hr. The wells were washed before

847 the addition of 100 μl/well of 3, 3', 5, 5'-tetramethylbenzidine (TMB, Sigma-Aldrich, Massachusetts,

848 USA) substrate at room temperature for 5 min. The colorimetric reaction was stopped by the addition

849 of 100 μl/well 1N HCl and the absorbance was detected by spectrophotometry at OD_{450} (Molecular

850 Device, California, USA). The absorbances at OD_{450} were plotted against the concentrations of His-

851 TvFACPα to generate Scatchard plots and calculate K_d and B_{max} values (54).

852

Actin biochemical fractionation

853

854 G- and F-actin were fractionated and enriched using a commercial *in vivo* assay biochem kit

855 (Cytoskeleton Inc, Colorado, USA), according to the manufacturer's instructions with minor

856 modifications. Briefly, around 3×10^7 trophozoites were incubated in cell lysis buffer (Cytoskeleton

857 Inc, Colorado, USA) with vigorous agitation at 4℃ for 30 min and homogenized by a 23-gauge needle

858 on a 5-ml syringe. The total lysate was centrifuged at $1,000 \times g$ to remove the unbroken cell debris,

859 followed by ultracentrifugation at $100,000 \times g$ for 1 hr to separate the insoluble F-actin and associated

860 proteins in the pellet from soluble G-actin in the supernatant. In western blotting, α-tubulin and TvCyP2

861 were respectively detected as purity markers for F-actin and G-actin fractions.

862

Cell migration assay

863

864 For the wound healing assay, adherent *T. vaginalis* trophozoites were cultured to a confluent

865 monolayer in a T25 flask. A scratch (200-μm to 1-mm wide) was generated by scraping the trophozoite

866 monolayer with a P200 tip. After removal of cell debris by washing once with the growth medium, the

867 culture flask was incubated at 37℃ and images were captured in a defined area at an interval of 30 min

868 over 2 hr. The wound closure area in each image was measured by ImageJ software (Version 1.53q,

869 National Institutes of Health, Maryland, USA). For the trans-well migration assay, $\sim 1 \times 10^7$

870 trophozoites suspended in 2 ml of TYI medium were inoculated into the top insert divided by a

871 polyester membrane with 3-μm pores (4.6 cm^2, JET Biofil, Guangzhou, China). The top insert was

872 placed in a 6-well culture plate containing 2 ml of TYI medium and cultured at 37 ℃ for 30 min. The

873   trophozoites in the top insert and bottom well were collected for microscopic observation and western

874   blotting.

875

876   **Statistical analysis**

877   Statistical significance of data collected from control and conditional samples was analyzed by

878   Microsoft Office Excel 2019 software with Student's t-test. $P < 0.05$ is considered as significant

879   difference.

880

881   **Acknowledgement**

889

890   **Author contributions**

891   Kai-Hsuan Wang: Investigation, Validation, and Methodology.

892   Jing-Yang Chang: Investigation, Validation, and Methodology.

893   Fu-An Li: Investigation, Validation, and Methodology.

894   Yen-Ju Chen: Investigation, Validation, and Methodology.

895   Kuan-Yi Wu: Investigation, Validation, and Methodology.

896   Tse-Ling Chu: Investigation and Validation

897   Jessica Lin: Investigation and Validation

898   Hong-Ming Hsu: Investigation, Validation, Project Administration, Supervision, Funding Acquisition,

899   Conceptualization, Writing-Original Draft Preparation, and Writing-Review & Editing.

900

901   **Statement of conflict of interest**

902   The authors declare that they have no competing interests in this manuscript.

903

904   **Data availability Section**

905   All data generated or analyzed during this study are included in the manuscript and supplementary data;

906   Source Data files have been provided for Table 1, the statistical analysis of quantification, and raw gel

907   or blot images generated in this study. The proteomics raw data have been deposited to Dryad

908   (https://datadryad.org/stash/share/e30mZQElM-nBNmJOniuiGSBJWBkB7V4-t0XzQ891cX8)   and

909   PRIDE (www.ebi.ac.uk/pride/) with a dataset identifier number PXD034359. (PRIDE Reviewer access

910   account details: Username: reviewer_pxd034359@ebi.ac.uk, Password: XpCqEnqW).

911

References

912

1. World Health Organization (2008) Global incidence and prevalence of selected curable sexually transmitted infections. ISBN 978 92 4 150383 9

2. Chen YP, Riestra AM, Rai AK, Johnson PJ (2019) A Novel Cadherin-like Protein Mediates Adherence to and Killing of Host Cells by the Parasite *Trichomonas vaginalis*. *mBio* 10(3):e00720-19

3. Riestra AM., Gandhi S, Sweredoski MJ, Moradian A, Hess S, Urban S, Johnson P J (2015) A *Trichomonas vaginalis* Rhomboid Protease and Its Substrate Modulate Parasite Attachment and Cytolysis of Host Cells. *PLoS pathogens* 11(12): e1005294

4. Rendón-Gandarilla FJ, Ramón-Luing Lde L, Ortega-López J, Rosa de Andrade I, Benchimol M, Arroyo R. (2013) The TvLEGU-1, a legumain-like cysteine proteinase, plays a key role in *Trichomonas vaginalis* cytoadherence. *Biomed Res Int* :561979. doi:10.1155/2013/561979

5. Pachano T, Nievas YR, Lizarraga A, Johnson PJ, Strobl-Mazzulla PH, de Miguel N (2017) Epigenetics regulates transcription and pathogenesis in the parasite *Trichomonas vaginalis*. *Cell Microbiol* 19(6):10.1111/cmi.12716. doi:10.1111/cmi.12716

6. Molgora BM, Rai AK, Sweredoski MJ, Moradian A, Hess S, Johnson PJ (2021) A Novel *Trichomonas vaginalis* Surface Protein Modulates Parasite Attachment via Protein:Host Cell Proteoglycan Interaction. *mBio* 12(1):e03374-20

7. Alderete JF, Nguyen J, Mundodi V, Lehker MW (2003) Heme-iron increases levels of AP65-mediated adherence by *Trichomonas vaginalis*. *Microb Pathog* 36(5):263-271. doi:10.1016/j.micpath..12.007

8. Alderete JF, O'Brien JL, Arroyo R, Engbring JA, Musatovova O, Lopez O, Lauriano C, Nguyen J (1995) Cloning and molecular characterization of two genes encoding adhesion proteins involved in *Trichomonas vaginalis* cytoadherence. *Mol Microbiol* 17(1):69-83. doi: 10.1111/j.1365-2958.1995.mmi_17010069.x.

9. O'Brien JL, Lauriano CM, Alderete JF (1996) Molecular characterization of a third malic enzyme-like AP65 adhesin gene of *Trichomonas vaginalis*. *Microb Pathog* 20(6):335-49. doi: 10.1006/mpat.1996.0032.

10. Moreno-Brito V, Yáñez-Gómez C, Meza-Cervantez P, Avila-González L, Rodríguez MA, Ortega-López J, González-Robles A, Arroyo R (2005) A *Trichomonas vaginalis* 120 kDa protein with identity to hydrogenosome pyruvate:ferredoxin oxidoreductase is a surface adhesin induced by iron. *Cell Microbiol* 7(2):245-58. doi: 10.1111/j.1462-5822.2004.00455.x.

11. Wu C (2007) Focal adhesion: a focal point in current cell biology and molecular medicine. *Cell Adh Migr* 1(1):13-18. doi:10.4161/cam.1.1.4081.

12. Fournier MF, Sauser R, Ambrosi D, Meister JJ, Verkhovsky AB (2010) Force transmission in migrating cells. *J Cell Biol* 188(2):287-297. doi:10.1083/jcb.200906139.

13. Bachir AI, Horwitz AR, Nelson WJ, Bianchini JM (2017) Actin-Based Adhesion Modules Mediate Cell Interactions with the Extracellular Matrix and Neighboring Cells. *Cold Spring Harb Perspect Biol* 9(7):a023234.

35

14. Casta e Silva Filho F, de Souza W, Lopes JD (1988) Presence of laminin-binding proteins in trichomonads and their role in adhesion. *Proc Natl Acad Sci U S A* 85(21):8042-8046. doi:10.1073/pnas.85.21.8042

15. Huang KY, Huang PJ, Ku FM, Lin R, Alderete JF, Tang P (2012) Comparative transcriptomic and proteomic analyses of *Trichomonas vaginalis* following adherence to fibronectin. *Infect Immun* 80(11):3900-3911. doi:10.1128/IAI.00611-12

16. Lama A, Kucknoor A, Mundodi V, Alderete JF (2009) Glyceraldehyde-3-phosphate dehydrogenase is a surface-associated, fibronectin-binding protein of *Trichomonas vaginalis*. *Infect Immun* 77(7):2703-2711. doi:10.1128/IAI.00157-09

17. Dos Santos O, Rigo GV, Macedo AJ, Tasca T (2017) *Trichomonas vaginalis* clinical isolates: cytoadherence and adherence to polystyrene, intrauterine device, and vaginal ring. *Parasitol Res* 116(12):3275-3284. doi:10.1007/s00436-017-5638-0

18. Arroyo R, González-Robles A, Martínez-Palomo A, Alderete JF (1993) Signalling of *Trichomonas vaginalis* for amoeboid transformation and adhesion synthesis follows cytoadherence. *Mol Microbiol* 7(2):299-309. doi:10.1111/j.1365-2958.1993.tb01121.x

19. Velle KB, Fritz-Laylin LK (2020) Conserved actin machinery drives microtubule-independent motility and phagocytosis in *Naegleria*. *J Cell Biol* 219(11):e202007158. doi:10.1083/jcb.202007158

20. Sohn HJ, Song KJ, Kang H, Ham AJ, Lee JH, Chwae YJ, Kim K, Park S, Kim JH, Shin HJ (2019) Cellular characterization of actin gene concerned with contact-dependent mechanisms in *Naegleria fowleri*. *Parasite Immunol* 41(8):e12631. doi: 10.1111/pim.12631

21. Pollard TD, Cooper JA (2009) Actin, a central player in cell shape and movement. *Science* 326(5957):1208-1212. doi:10.1126/science.1175862

22. Friedl P, Bröcker EB (2000) The biology of cell locomotion within three-dimensional extracellular matrix. *Cell Mol Life Sci* 57(1):41-64. doi:10.1007/s000180050498

23. Parsons JT, Horwitz AR, Schwartz MA (2010) Cell adhesion: integrating cytoskeletal dynamics and cellular tension. *Nat Rev Mol Cell Biol* 11(9):633-643. doi:10.1038/nrm2957

24. Mullins RD, Heuser JA, Pollard TD (1998) The interaction of Arp2/3 complex with actin: nucleation, high affinity pointed end capping, and formation of branching networks of filaments. *Proc Natl Acad Sci U S A* 95(11):6181-6186. doi:10.1073/pnas.95.11.6181.

25. Tang DD, Gerlach BD (2017) The roles and regulation of the actin cytoskeleton, intermediate filaments and microtubules in smooth muscle cell migration. Respir Res. 2017;18(1):54. doi:10.1186/s12931-017-0544-7

26. Bearer EL (1993) Role of actin polymerization in cell locomotion: molecules and models. *Am J Respir Cell Mol Biol* 8(6):582-591. doi:10.1165/ajrcmb/8.6.582

27. Funk J, Merino F, Schaks M, Rottner K, Raunser S, Bieling P (2021) A barbed end interference mechanism reveals how capping protein promotes nucleation in branched actin networks. *Nat Commun* 12(1):5329. doi:10.1038/s41467-021-25682-5

28. Wear MA, Yamashita A, Kim K, Maéda Y, Cooper JA (2003) How capping protein binds the barbed

end of the actin filament. *Curr Biol* 13(17):1531-1537. doi:10.1016/s0960-9822(03)00559-1

29. Kim K, Yamashita A, Wear MA, Maéda Y, Cooper JA (2004) Capping protein binding to actin in yeast: biochemical mechanism and physiological relevance. *J Cell Biol* 164(4):567-580. doi:10.1083/jcb.200308061

30. Hernandez-Valladares M, Kim T, Kannan B, Tung A, Aguda AH, Larsson M, Cooper JA, Robinson RC (2010) Structural characterization of a capping protein interaction motif defines a family of actin filament regulators. *Nat Struct Mol Biol* 17(4):497-503. doi: 10.1038/nsmb.1792

31. Edwards M, Zwolak A, Schafer DA, Sept D, Dominguez R, Cooper JA (2014) Capping protein regulators fine-tune actin assembly dynamics. *Nat Rev Mol Cell Biol* 15(10):677-689. doi:10.1038/nrm3869

32. Solís C, Russell B (2021) Striated muscle proteins are regulated both by mechanical deformation and by chemical post-translational modification. *Biophys Rev* 13(5):679-695. doi:10.1007/s12551-021-00835-4

33. Canton DA, Olsten ME, Kim K, Doherty-Kirby A, Lajoie G, Cooper JA, Litchfield DW (2005) The pleckstrin homology domain-containing protein CKIP-1 is involved in regulation of cell morphology and the actin cytoskeleton and interaction with actin capping protein. *Mol Cell Biol* 25(9):3519-34. doi: 10.1128/MCB.25.9.3519-3534.2005

34. Canton DA, Olsten ME, Niederstrasser H, Cooper JA, Litchfield DW (2006) The role of CKIP-1 in cell morphology depends on its interaction with actin-capping protein. *J Biol Chem* 281(47):36347-59. doi: 10.1074/jbc.M607595200.

35. Kusdian G, Woehle C, Martin WF, Gould SB (2013) The actin-based machinery of *Trichomonas vaginalis* mediates flagellate-amoeboid transition and migration across host tissue. *Cell Microbiol* 15(10):1707-1721. doi:10.1111/cmi.12144

36. Vandekerckhove J, Deboben A, Nassal M, Wieland T (1985) The phalloidin binding site of F-actin. *EMBO J* 4(11):2815-2818. PMID: 4065095; PMCID: PMC554583.

37. Weichhart T, Haidinger M, Hörl WH, Säemann MD (2008) Current concepts of molecular defence mechanisms operative during urinary tract infection. *Eur J Clin Invest* 38 Suppl 2:29-38. doi:10.1111/j.1365-2362.2008.02006.x

38. Carlton JM, Hirt RP, Silva JC, Delcher AL, Schatz M, Zhao Q, Wortman JR, Bidwell SL, Alsmark UC, Besteiro S, Sicheritz-Ponten T *et al* (2007) Draft genome sequence of the sexually transmitted pathogen *Trichomonas vaginalis*. *Science* 315(5809):207-212. doi:10.1126/science.1132894

39. Davidson PM, Cadot B (2021) Actin on and around the Nucleus. *Trends Cell Biol* 31(3):211-223. doi:10.1016/j.tcb.2020.11.009

40. Falck S, Paavilainen VO, Wear MA, Grossmann JG, Cooper JA, Lappalainen P. (2004) Biological role and structural mechanism of twinfilin-capping protein interaction. *EMBO J* 23(15):3010-3019. doi:10.1038/sj.emboj.7600310

41. Yuan A, Mills RG, Bamburg JR, Bray JJ (1999) Cotransport of glyceraldehyde-3-phosphate dehydrogenase and actin in axons of chicken motoneurons. *Cell Mol Neurobiol* 19(6):733-744.

1029   doi:10.1023/a:1006953022763

1030 42. Choder M (2004) Rpb4 and Rpb7: subunits of RNA polymerase II and beyond. *Trends Biochem*
1031   *Sci* 29(12):674-681. doi:10.1016/j.tibs.2004.10.007

1032 43. Mitsuzawa H, Kimura M, Kanda E, Ishihama A (2005) Glyceraldehyde-3-phosphate
1033   dehydrogenase and actin associate with RNA polymerase II and interact with its Rpb7
1034   subunit. *FEBS Lett* 579(1):48-52. doi:10.1016/j.febslet.2004.11.045

1035 44. Battistutta R, De Moliner E, Sarno S, Zanotti G, Pinna LA (2001) Structural features underlying
1036   selective inhibition of protein kinase CK2 by ATP site-directed tetrabromo-2-benzotriazole. *Protein*
1037   *Sci* 10(11):2200-2206. doi:10.1110/ps.19601

1038 45. Cable BL, John DT (1986) Conditions for maximum enflagellation in *Naegleria fowleri*. *J*
1039   *Protozool* 33(4):467-72. doi: 10.1111/j.1550-7408.1986.tb05643.x

1040 46. Yuyama S (1971) The effects of selected chemical agents on the amoeba-flagellate transformation
1041   in *Naegleria gruberi*. *J Protozool* 18(2):337-343. doi:10.1111/j.1550-7408.1971.tb03328.x

1042 47. Willmer EN. (1961) Amoeba-flagellate transformation. *Exp Cell Res* Suppl 8:32-46.
1043   doi:10.1016/0014-4827(61)90338

1044 48. Hsu HM, Lee Y, Hsu PH, Liu HW, Chu CH, Chou YW, Chen YR, Chen SH, Tai JH (2014) Signal
1045   transduction triggered by iron to induce the nuclear importation of a Myb3 transcription factor in
1046   the parasitic protozoan *Trichomonas vaginalis*. *J Biol Chem* 289(42):29334-29349.
1047   doi:10.1074/jbc.M114.599498

1048 49. Fuhrmann A, Engler AJ (2015) The cytoskeleton regulates cell attachment strength. *Biophys J*
1049   109(1):57-65. doi:10.1016/j.bpj.2015.06.003

1050 50. Hsu HM, Huang YH, Aryal S, Liu HW, Chen C, Chen SH, Chu CH, Tai JH (2020) Endomembrane
1051   Protein Trafficking Regulated by a TvCyP2 Cyclophilin in the Protozoan Parasite, *Trichomonas*
1052   *vaginalis*. *Sci Rep* 10(1):1275. doi:10.1038/s41598-020-58270-6

1053 51. Neace CJ, Alderete JF (2013) Epitopes of the highly immunogenic *Trichomonas vaginalis* α-actinin
1054   are serodiagnostic targets for both women and men. *J Clin Microbiol* 51(8):2483-2490.
1055   doi:10.1128/JCM.00582-13

1056 52. Perez-Riverol, Y, Bai, J, Bandla, C, García-Seisdedos, D, Hewapathirana, S, Kamatchinathan, S,
1057   Kundu, DJ, Prakash, A, Frericks-Zipper, A, Eisenacher, M, Walzer, M, Wang, S, Brazma, A,
1058   Vizcaíno, JA (2022) The PRIDE database resources in 2022: a hub for mass spectrometry-based
1059   proteomics evidences. *Nucleic acids research*, *50*(D1), D543–D552. doi: 10.1093/nar/gkab1038..

1060 53. Hatano T, Alioto S, Roscioli E, Palani S, Clarke ST, Kamnev A, Hernandez-Fernaud JR,
1061   Sivashanmugam L, Chapa-Y-Lazo B, Jones AME *et al* (2018) Rapid production of pure
1062   recombinant actin isoforms in *Pichia pastoris*. *J Cell Sci* 131(8):jcs213827.
1063   doi:10.1242/jcs.213827

1064 54. He HJ, Wang XS, Pan R, Wang DL, Liu MN, He RQ (2009) The proline-rich domain of tau plays
1065   a role in interactions with actin. *BMC Cell Biol* 10:81. doi:10.1186/1471-2121-10-81

1066

1067

1068 **Table 1. The list of *Tv*actin-interacted proteins identified by LC-MS/MS**

1069 The proteins identified by mass spectrometry with emPAI value above 0.25 or the peptides specific in

1070 the immunoprecipitant of HA-*Tv*actin were listed.

Accession	Score	Mass	emPAI	Description
Chaperone				
A2DS85	56	58182	0.15	T-complex protein 1 subunit delta, TVAG_066690
A2E9D9	62	58553	0.15	Chaperonin subunit alpha1 CCTalpha, putative, TVAG_364270
DNA/RNA-binding, or -regulatory protein				
A2DHC5	37	15204	0.31	Histone H2A OS=Trichomonas vaginalis, TVAG_021440
A2ELI6	46	11528	0.42	HTH myb-type domain-containing protein, TVAG_257520
A2D755	78	127201	0.1	DEAD/DEAH box helicase family protein, TVAG_119080
Cytoskeletal protein				
A2FE30	541	29551	9.69	F-actin-capping protein subunit alpha, TVAG_470230
A2E0V9	104	46956	0.3	Actin-like protein 3, putative, TVAG_371880
A2E755	69	533676	0.02	Dynein heavy chain family protein, TVAG_006480
A2EIJ3	43	48424	0.19	Coronin, TVAG_124870
A2DC16	208	50493	0.51	Tubulin beta chain, TVAG_008680
A2EGW8	73	515283	0.02	Dynein heavy chain family protein, TVAG_497260
A2GKR2	363	26669	5.37	Actin (Fragment), TVAG_534990
P90623	659	42154	9.49	Actin, TVAG_337240
A2DKH3	163	106648	0.21	Alpha-actinin, putative, TVAG_190450
Membrane traffic protein				
A2EV08	90	85200	0.1	Clathrin and VPS domain-containing protein, TVAG_369030
Metabolite interconversion enzyme				
A2DSX4	80	107447	0.21	Alpha-1,4 glucan phosphorylase, TVAG_348330
A2EBX0	218	44060	0.76	Succinate--CoA ligase [ADP-forming] subunit beta, mitochondrial, TVAG_259190
A2FR66	116	35697	0.26	6-phosphofructokinase, TVAG_496160
A2E9H3	37	47022	0.19	Pyrophosphate--fructose 6-phosphate 1-phosphotransferase 2, TVAG_364620
A2FVK7	224	44039	1.12	Succinate--CoA ligase [ADP-forming] subunit beta, mitochondrial, TVAG_144730
A2DM03	169	34697	0.61	6-phosphofructokinase, TVAG_462920
A2FKA7	82	34780	0.27	6-phosphofructokinase, TVAG_293770
A2EM29	503	39758	6.2	Glyceraldehyde-3-phosphate dehydrogenase, TVAG_475220
Q27088	86	129430	0.1	Pyruvate:ferredoxin oxidoreductase A, TVAG_198110
A2EAJ8	98	42785	0.47	Malic enzyme, TVAG_491670
A2DM76	95	38889	0.11	Thymidine kinase, TVAG_083490
A2D987	238	44049	1.33	Succinate--CoA ligase [ADP-forming] subunit beta, mitochondrial, TVAG_183500
A2DFT9	198	35079	1.02	6-phosphofructokinase, TVAG_391760
A2F259	111	109764	0.16	Amylomaltase, TVAG_154680
A2D7H3	94	110021	0.08	Amylomaltase, TVAG_120280

Protein modifying enzyme				
A2EPF2	49	95046	0.09	Proteasome/cyclosome repeat family protein, TVAG_286380
Protein-binding activity modulator				
A2EB65	53	40705	0.22	G-protein alpha subunit, putative, TVAG_274750
A2EJL0	36	24328	0.18	IBD domain-containing protein, TVAG_197940
Translation protein				
A2E4D0	39	40574	0.11	Ribosomal protein, putative, TVAG_128790
A2DSF6	55	48559	0.19	Elongation factor 1-alpha, TVAG_067400
A2ECS2	117	94235	0.36	Tr-type G domain-containing protein, TVAG_276410
A2DSV0	99	28352	0.34	Ribosomal protein S3Ae, putative, TVAG_348090
Transporter				
A2FS41	70	49238	0.18	V-ATPase_H_C domain-containing protein, TVAG_262750
A2ED49	68	68309	0.2	H(+)-transporting two-sector ATPase, TVAG_420260
A2ES57	50	55789	0.41	Vacuolar proton pump subunit B, TVAG_453110
Uncharacterized protein				
A2E2D0	59	149814	0.06	Uncharacterized protein, TVAG_098000

1071

1072 **Supplement data and legends**

1073

1074 **Figure 2-Figure Supplement 1.**

Fig 2. S1
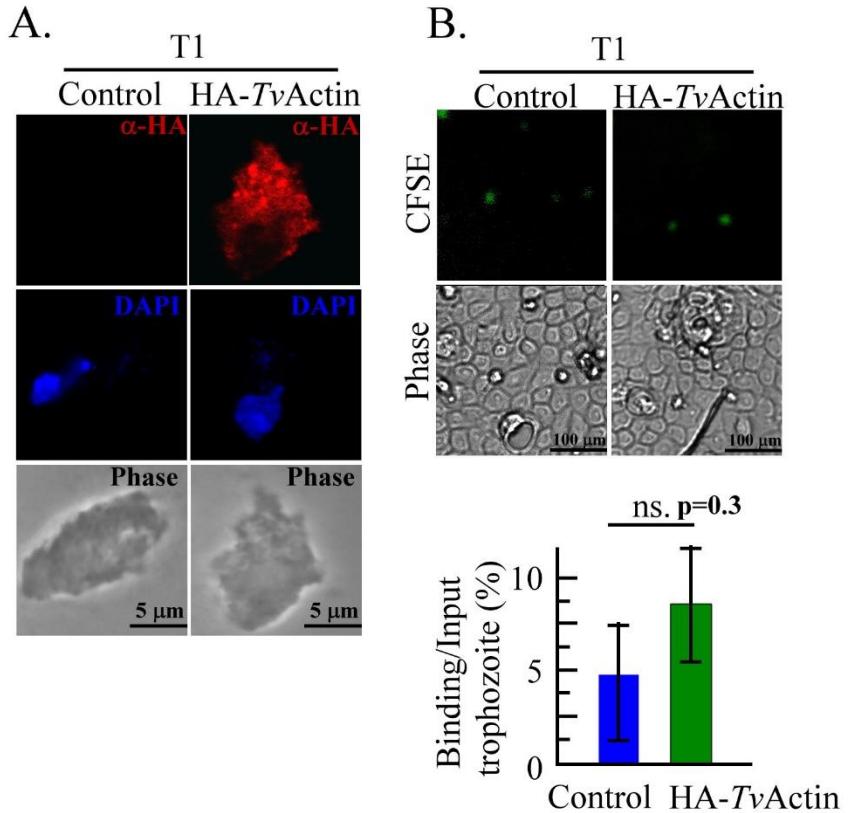
1075

1076 **Figure 2-Figure Supplement 1. Overexpression of HA-*Tv*actin in nonadherent T1**

1077 **isolate.** (A.) The non-transgenic and HA-*Tv*actin transgenic T1 trophozoites were fixed for

1078 IFA by an anti-HA antibody and then incubated with a Cy3-conjugated secondary antibody.

1079 The nuclei were stained by DAPI and the morphology was observed by phase-contrast

1080 microscopy. The scale bars represent 5 μm. (B.) The non-transgenic and HA-*Tv*actin

1081 transgenic T1 trophozoites prelabeled by CFSE were co-cultured with *h*VECs at MOI of 2:1

1082 for 1 hr in the cytoadherence binding assay. The scale bars represent 100 μm. The assays

1083 were repeated three times. Data in the histogram are presented as mean ± SEM. Significance

1084 with p-value is statistically analyzed by Student's t-test as indicated. (n=3, P<0.01, P<0.05,

1085 and ns, no significance).

1086

1087

1088

1089

1090

41

1091 **Figure 2-Figure Supplement 2.**

Fig 2. S2
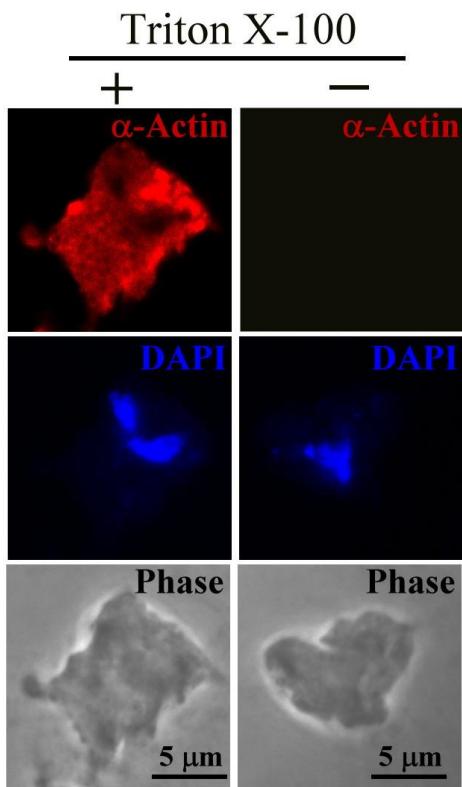
1092

1093 **Figure 2-Figure Supplement 2. No detectable α-actin on the cell surface of _T. vaginalis_.**

1094 The TH17 trophozoites with or without Triton X-100 permeation were examined by IFA using

1095 an anti-α-actin antibody, followed by incubation with a Cy3-conjugated secondary antibody.

1096 The nuclei were stained by DAPI. The morphology was observed by phase-contrast

1097 microscopy. The scale bars represent 5 μm.

1098

1099

1100

1101

1102

1103

1104

1105 **Figure 2-Figure Supplement 3.**

1106

1107 **Figure 2-Figure Supplement 3. Protein sequence alignment of α-actin and *Tv*FACPα.**
1108 (A.) The full-length protein sequences of α-actin from human (*h*Actin, P68133), mouse
1109 (*m*Actin, P68134), yeast (*y*Actin, P60010), and *T. vaginalis* (*Tv*Actin, TVAG_337240) were
1110 aligned to show the protein sequence similarity. The conserved amino acid residues are
1111 highlighted, and the binding sites of phalloidin or LatB in α-actin are indicated by P or L as
1112 shown at the top of sequences, respectively.

1113

43

1114 **Figure 4-Figure Supplement 1.**

Fig 4. S1
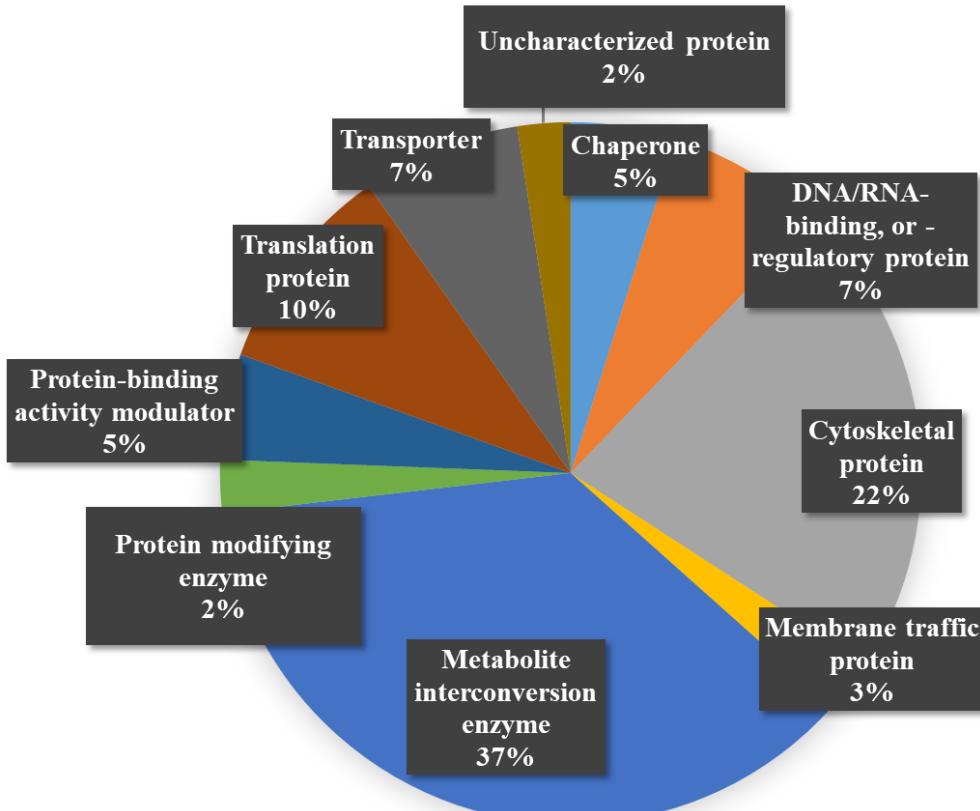
1115

1116 **Figure 4-Figure Supplement 1. Protein function category.** The mass identified proteins

1117 were classified by function into multiple cellular pathways, including cytoskeleton proteins

1118 (22%), chaperones (5%), membrane trafficking (3%), transporter (7%), protein binding (5%),

1119 modification (2%), DNA/RNA regulation (7%) and translation (10%), metabolism enzymes

1120 (37%), and uncharacterized proteins (2%).

1121

1122

1123 **Figure 4-Figure Supplement 2.**

Fig 4. S2
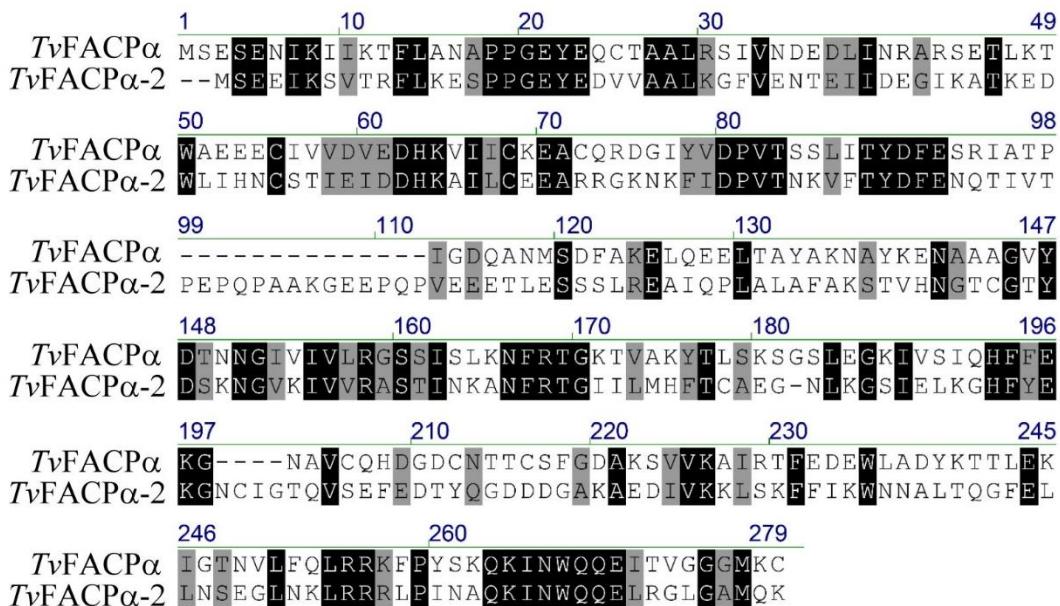
1124

1125 **Figure 4-Figure Supplement 2. The sequence alignment for *Tv*FACPs in *T. vaginalis.* The**

1126 protein sequences of *Tv*FACPα (TVAG_470230) and *Tv*FACPα-2 (TVAG_212270) were aligned.

1127 The conserved amino acid residues are highlighted.

1128

1129 **Figure 7-Figure Supplement 1.**
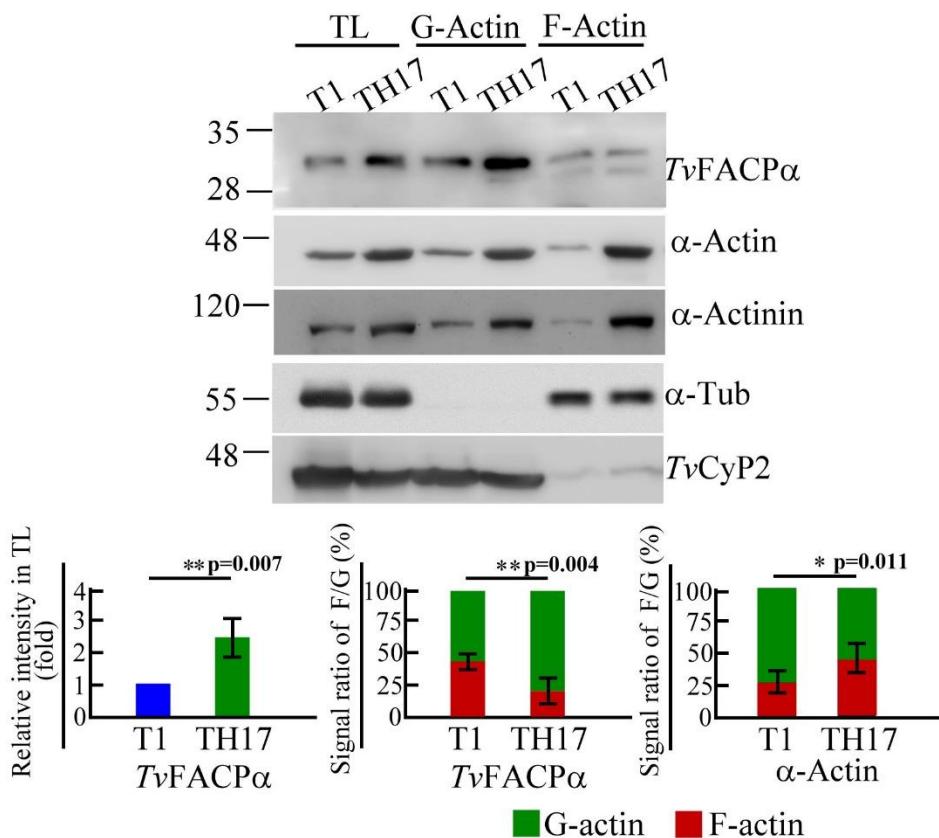
1130

1131 **Figure 7-Figure Supplement 1. Differential expression of *Tv*FACPα in nonadherent and**
1132 **adherent isolates of *T. vaginalis.*** The protein lysates from Figure 2E were re-examined by
1133 western blotting with the anti-*Tv*FACPα antibody. The relative intensity of *Tv*FACPα detected
1134 in total lysate, the signal ratio of *Tv*FACPα in F-actin versus G-actin fractions were shown in
1135 the histograms. The assays were repeated three times. Data in histograms are presented as mean
1136 ± SEM. Significance with p-value is statistically analyzed by Student's t-test as indicated. (n=3,
1137 P<0.01, P<0.05, and ns, no significance).

1138

1139   **Figure 9-Figure Supplement 1.**

Fig 9. S1

5 μm
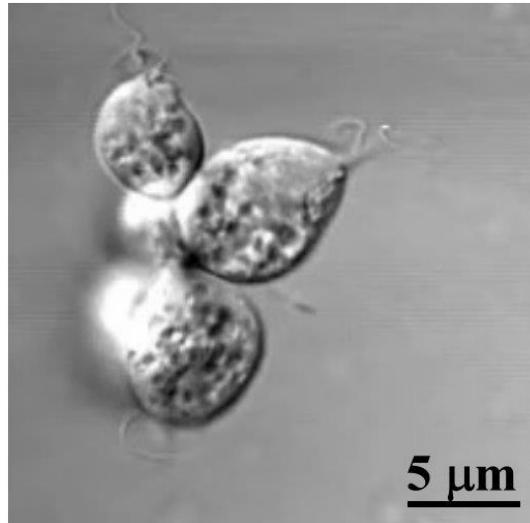
1140

1141   **Figure 9-Figure Supplement 1. Morphology of trophozoites in the bottom well of trans-**

1142   **well assay.** Morphology of trophozoites migrating into the bottom well was recorded by

1143   microscopy. The parasite in the bottom well were observed in dominant flagellate trophozoite

1144   with clear flagella under our assay conditions. The scale bar represents 5 μm.

1145

1146

1147

1   **Supplement data and legends**

Fig 2. S1
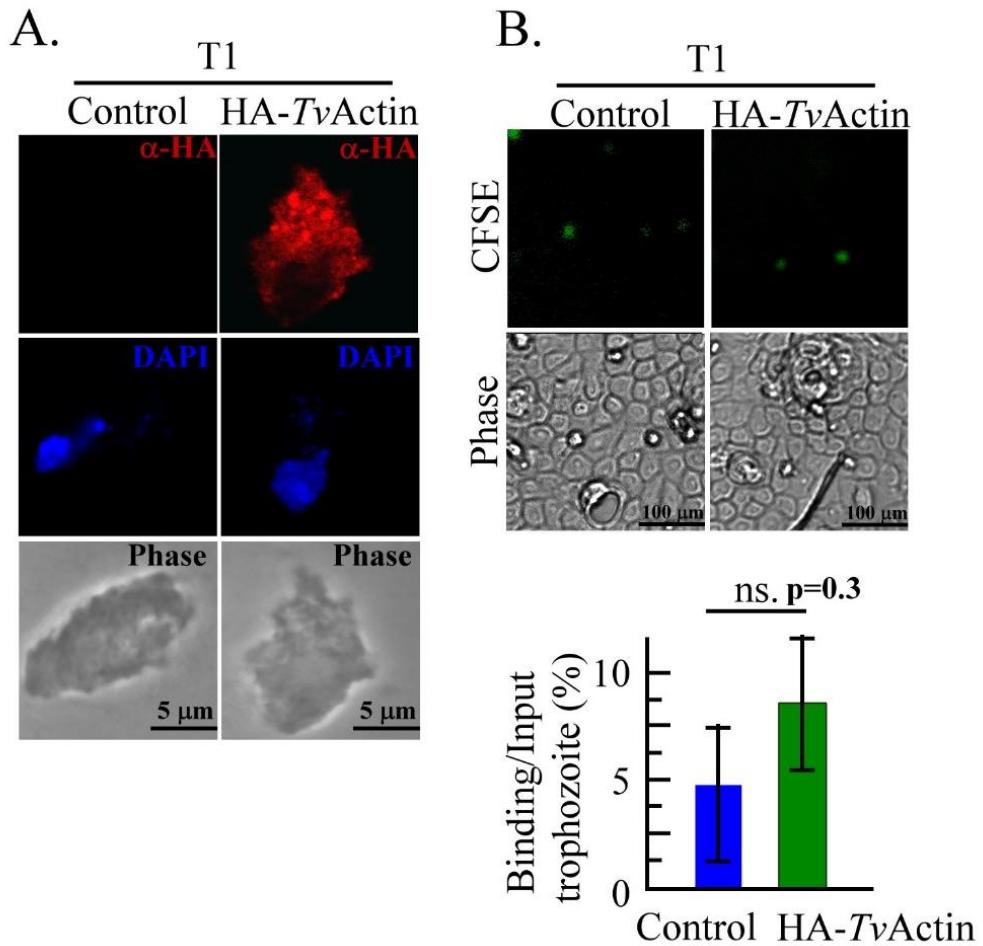
2

3   **Figure 2-Figure Supplement 1. Overexpression of HA-*Tv*actin in nonadherent T1**

4   **isolate.** (A.) The non-transgenic and HA-*Tv*actin transgenic T1 trophozoites were fixed

5   for IFA by an anti-HA antibody and then incubated with a Cy3-conjugated secondary

6   antibody. The nuclei were stained by DAPI and the morphology was observed by phase-

7   contrast microscopy. The scale bars represent 5 μm. (B.) The non-transgenic and HA-

8   *Tv*actin transgenic T1 trophozoites prelabeled by CFSE were co-cultured with *h*VECs

9   at MOI of 2:1 for 1 hr in the cytoadherence binding assay. The scale bars represent 100

10   μm.   The assays were repeated three times. Data in the histogram are presented as

11   mean ± SEM. Significance with p-value is statistically analyzed by Student's t-test as

12   indicated. (n=3, P<0.01, P<0.05, and ns, no significance).

13

Fig 2. S2
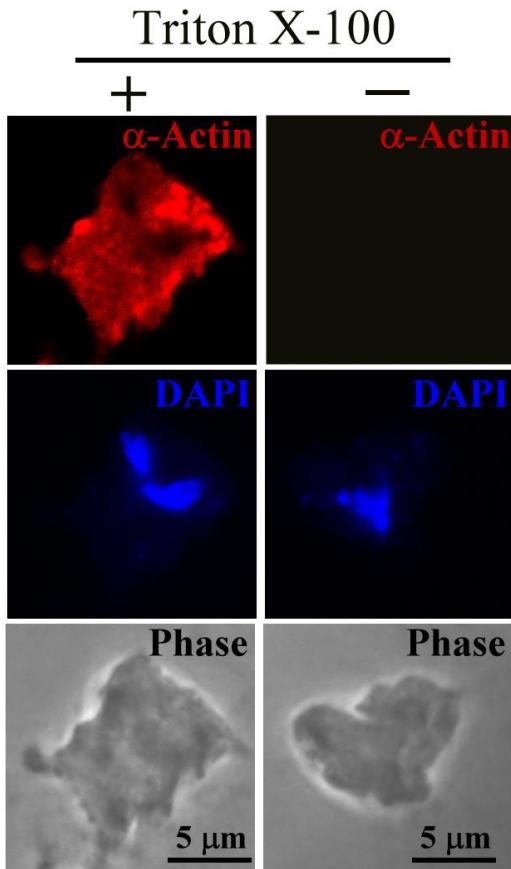
Triton X-100

+   **−**

α-Actin   α-Actin

DAPI   DAPI

Phase   Phase

5 μm   5 μm

14

Figure 2-Figure Supplement 2. No detectable α-actin on the cell surface of *T. vaginalis*. The TH17 trophozoites with or without Triton X-100 permeation were examined by IFA using an anti-α-actin antibody, followed by incubation with a Cy3-conjugated secondary antibody. The nuclei were stained by DAPI. The morphology was observed by phase-contrast microscopy. The scale bars represent 5 μm.

Fig 2. S3

20
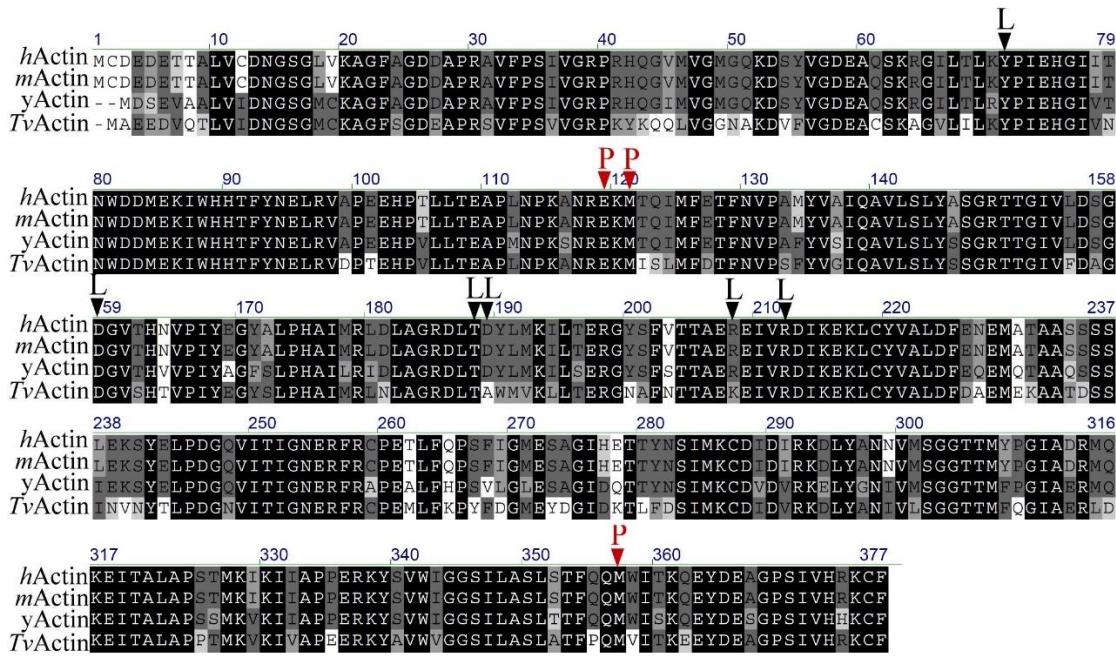
Figure 2-Figure Supplement 3. Protein sequence alignment of α-actin and *Tv*FACPα. (A.) The full-length protein sequences of α-actin from human (*h*Actin, P68133), mouse (mActin, P68134), yeast (yActin, P60010), and *T. vaginalis* (*Tv*actin, TVAG_337240) were aligned to show the protein sequence similarity. The conserved amino acid residues are highlighted, and the binding sites of phalloidin or LatB in α-actin are indicated by P or L as shown at the top of sequences, respectively.

Fig 4. S1
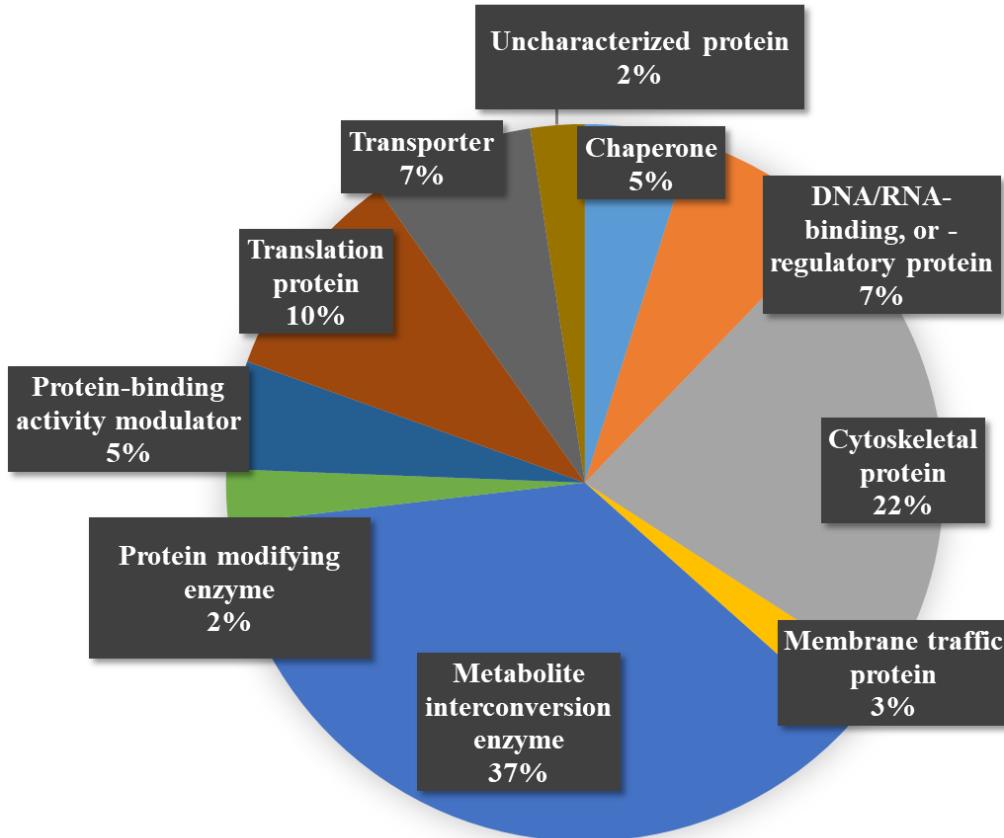
27

Figure 4-Figure Supplement 1. Protein function category. The mass identified proteins were classified by function into multiple cellular pathways, including cytoskeleton proteins (22%), chaperones (5%), membrane trafficking (3%), transporter (7%), protein binding (5%), modification (2%), DNA/RNA regulation (7%) and translation (10%), metabolism enzymes (37%), and uncharacterized proteins (2%).

Fig 4. S2
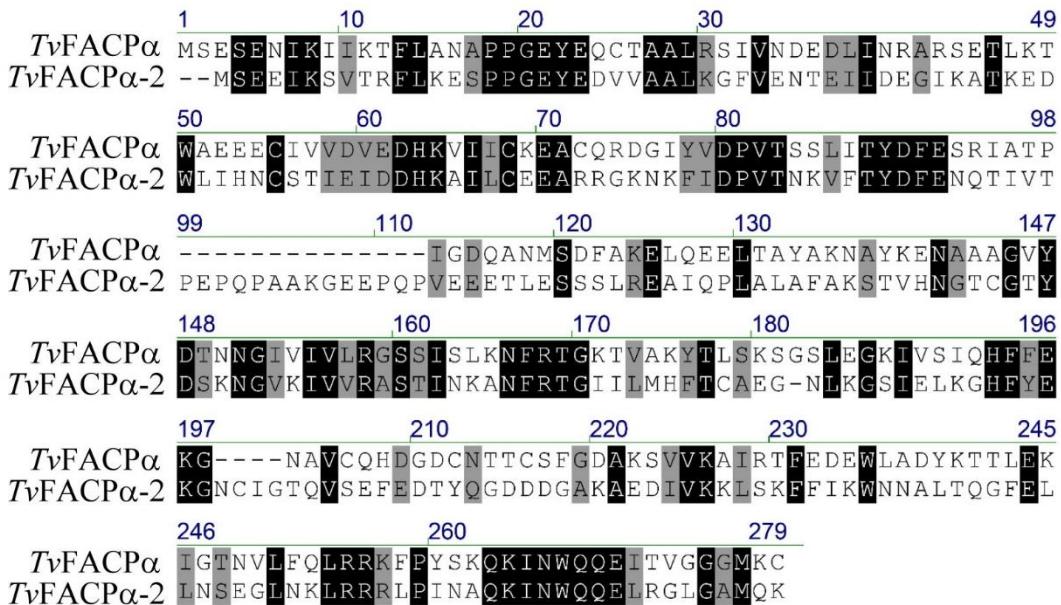
33

Figure 4-Figure Supplement 2. The sequence alignment for *Tv*FACPs in *T. vaginalis.* The protein sequences of *Tv*FACPα (TVAG_470230) and *Tv*FACPα-2 (TVAG_212270) were aligned. The conserved amino acid residues are highlighted.

Fig 7. S1
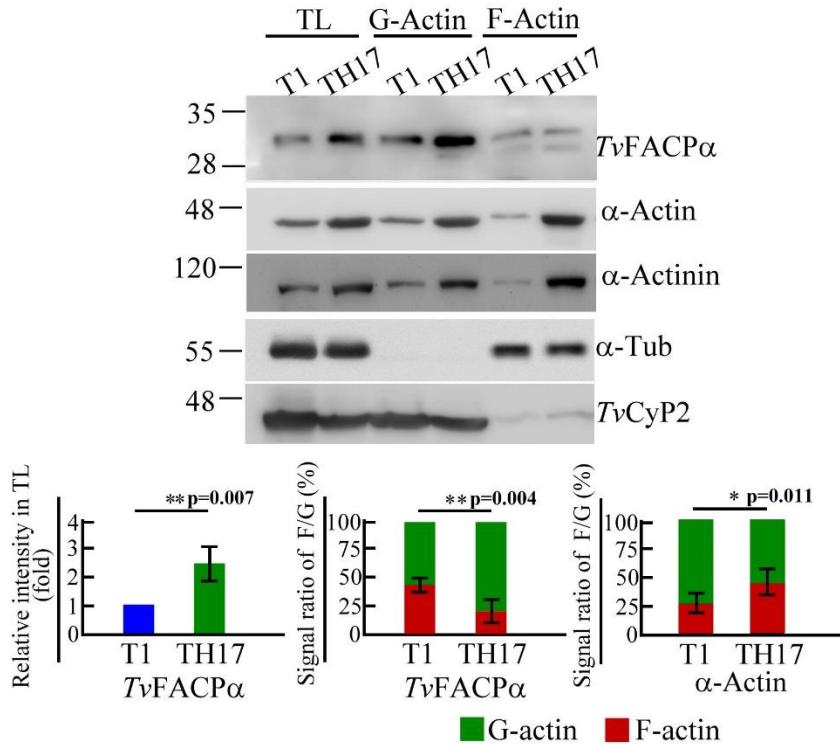
**Figure 7-Figure Supplement 1. Differential expression of *Tv*FACPα in nonadherent and adherent isolates of *T. vaginalis.* The protein lysates from Fig. 2E were re-examined by western blotting with the anti-*Tv*FACPα antibody. The relative intensity of *Tv*FACPα detected in total lysate, the signal ratio of *Tv*FACPα in F-actin versus G-actin fractions were shown in the histograms. The assays were repeated three times. Data in histograms are presented as mean ± SEM. Significance with p-value is statistically analyzed by Student's t-test as indicated. (n=3, $P<0.01$, $P<0.05$, and ns, no significance).

Fig 9. S1
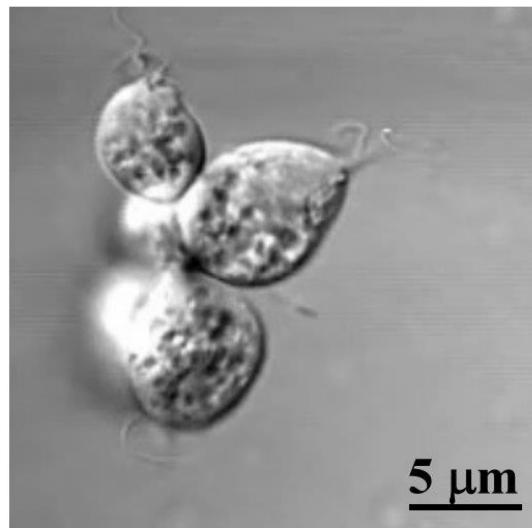
46

47 **Figure 9-Figure Supplement 1. Morphology of trophozoites in the bottom well of**

48 **trans-well assay.** Morphology of trophozoites migrating into the bottom well was

49 recorded by microscopy. The trophozoites in the bottom well were observed in

50 dominant flagellate form with clear flagella under our assay conditions. The scale bar

51 represents 5 μm.